Electrical Transport in Single-Wall Carbon Nanotubes

Michael J. Biercuk[1,3], Shahal Ilani[2], Charles M. Marcus[3], and Paul L. McEuen[2]

[1] Booz Allen Hamilton
Arlington, VA 22203, USA
[2] Laboratory of Atomic and Solid State Physics, Cornell University
Ithaca, NY 14853, USA
shahal.ilani@cornell.edu
mceuen@ccmr.cornell.edu
[3] Department of Physics, Harvard University
Cambridge, MA 02138, USA
marcus@harvard.edu

Abstract. We review recent progress in the measurement and understanding of the electrical properties of individual metal and semiconducting single-wall carbon nanotubes. The fundamental scattering mechanisms governing the electrical transport in nanotubes are discussed, along with the properties of p–n and Schottky-barrier junctions in semiconductor tubes. The use of advanced nanotube devices for electronic, high-frequency, and electromechanical applications is discussed. We then examine quantum transport in carbon nanotubes, including the observation of quantized conductance, proximity-induced supercurrents, and spin-dependent ballistic transport. We move on to explore the properties of single and coupled carbon-nanotube quantum dots. Spin and orbital (isospin) magnetic moments lead to fourfold shell structure and unusual Kondo phenomena. We conclude with a discussion of unanswered questions and a look to future research directions.

1 Introduction and Basic Properties

Since the discovery of single-wall carbon nanotubes (SWNTs) fifteen years ago [1], electrical measurements of individual SWNTs have proven to be one of the most powerful probes of this novel 1D system. Figure 1 shows a schematic of a standard device geometry. A SWNT is directly connected to two metallic contacts (labeled source and drain), and is capacitively coupled to a third gate terminal that can change the charge density on the tube (or equivalently, shift the energy bands in the conducting channel). Measurements are performed by applying ac or dc voltages to the various terminals and measuring the resulting currents between source and drain.

The first transport measurements in nanotube devices were reported in 1997–1998 [2–5], and since then there have been thousands of papers published on the subject. Scientists and engineers have built upon the simple three-terminal device geometry presented above to produce increasingly com-

A. Jorio, G. Dresselhaus, M. S. Dresselhaus (Eds.): Carbon Nanotubes,
Topics Appl. Physics **111**, 455–493 (2008)

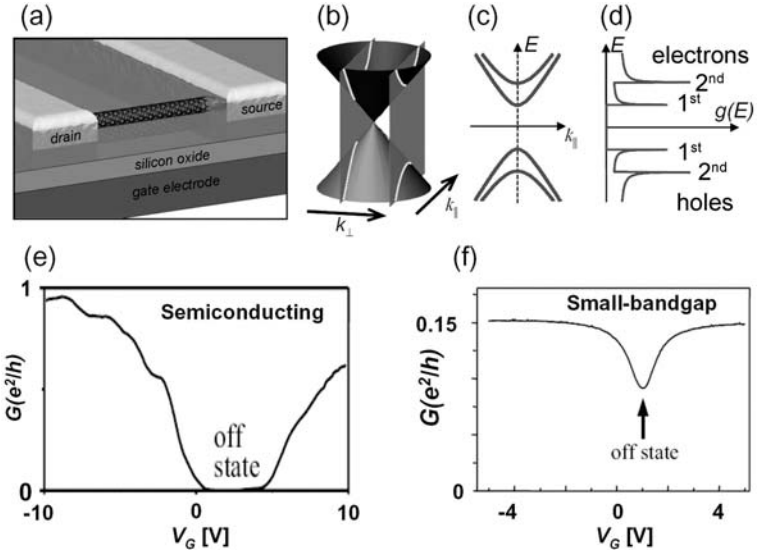

Fig. 1. (**a**) Schematic view a nanotube field-effect transistor (**b**) The Dirac energy dispersion cone of graphene near the K point in reciprocal space showing cutting lines for a semiconducting tube. (**c**) The dispersion relation of the semiconducting nanotube 1D subbands derived by slicing the cone at quantized values of the momentum along the circumference of the tube, $k_\perp$. (**d**) The corresponding 1D density of states. (**e**) Measured conductance of a semiconducting tube, G, as a function of gate voltage, V_g. (**f**) Same for small-bandgap metallic nanotube. Reference: McEuen group, unpublished

plex devices and to address questions of both device performance and fundamental physics. A decade later, a remarkably complete and consistent picture of transport in this novel 1D system has emerged. The power of transport measurements in elucidating the basic electronic properties of this material system has been truly remarkable. In this review, we summarize many of the major accomplishments, focusing on topics where a broad consensus has emerged and ones that were not covered in the previous book [6, 7]. We start with a discussion of the basic band structure and transport properties of nanotubes. In Sect. 2, we address the properties of nanotubes operating in the "classical", or incoherent, transport regime, and in Sect. 3 we discuss devices operating in this regime. In Sect. 4, we address the quantum properties of nanotube electrical transport and turn to nanotube quantum dots in Sect. 5. We end in Sect. 6 with a discussion of future research directions.

1.1 Band Structure

The transport properties of nanotubes are intimately related to their electronic band structure (see the contribution by Spataru et al.). The band

structure is composed of multiple 1D subbands sliced from the Dirac dispersion cone of graphene (Fig. 1b). These subbands have relativistic dispersion relations, which for the ith electron–hole subband are given by:

$$E_i(k) = \pm\left[(\hbar v_\mathrm{F} k)^2 + (E_\mathrm{g}^i/2)^2\right]^{1/2} . \tag{1}$$

Here, E and k are measured from the center of the Dirac cone of graphene, $v_\mathrm{F} \approx 8 \times 10^5\,\mathrm{m/s}$ is the Fermi velocity, and E_g^i are the individual energy gaps determined by the distance of the quantized k states to the center of the Dirac cone. The corresponding density of states, $g(E)$, has distinctive 1D van Hove singularities (Fig. 1d), and is given by:

$$g(E) = \sum_i g_i(E)\,, \qquad g_i(E) = \frac{4}{\pi\hbar v_\mathrm{F}}\left[1 - (E_\mathrm{g}^i/2E)^2\right]^{-1/2} . \tag{2}$$

The factor 4 in (2) comes from the fourfold degeneracy of each of these subbands at zero magnetic field, due to both the spin degeneracy and the orbital or "isospin" degeneracy associated with the band structure of graphene which is further discussed in the contribution by Charlier et al. This latter effect can be pictured as the separate left- and right-handed electron states spiraling down the tube. This fourfold degeneracy is lifted in a magnetic field by the orbital and spin Zeeman effects:

$$\Delta E_\mathrm{g}^i = -(\boldsymbol{\mu}_0 + \boldsymbol{\mu}_\mathrm{s}) \;\; \boldsymbol{B} = \pm\frac{d_\mathrm{t} e v_\mathrm{F} B_\parallel}{4} \pm \tfrac{1}{2}\, g\mu_b B_\mathrm{tot}\,, \tag{3}$$

where $B_\parallel$ is the field parallel to the tube axis, d_t is the tube diameter, g is the electrons' g-factor and B_tot is the total field. Nanotubes fall into three distinct electronic classes according to their fundamental bandgap, E_g^0, or simply E_g:

Semiconducting nanotubes, with a bandgap predicted by band theory to be $E_\mathrm{g} \approx 0.7\,\mathrm{eV}/d_\mathrm{t}(\mathrm{nm})$.
Small-bandgap nanotubes, which are nominally metallic tubes with a small bandgap (typically less than 100 mV) due to perturbations, such as curvature, strain, twist, etc.
True metallic nanotubes, where $E_\mathrm{g} = 0$. This class is rare, since nearly all tubes possess some small bandgap due to curvature, strain, or twist. These are often lumped together with small bandgap tubes, with the combined set called "metallic."

Three-terminal conductance measurements provide a direct means for identifying members of the different classes outlined above. The lower panels of Fig. 1 show the conductance measured at room temperature as a function of applied gate voltage for a semiconducting and a small-bandgap tube. When the Fermi level is tuned into the bandgap, the semiconducting tube shows

a broad region of near-zero conductance since $E_g \gg k_B T$, while the small-bandgap tube shows only a moderate dip since its bandgap is comparable to the thermal energy, $E_g \sim k_B T$.

Measurement of the nanotube capacitance to the gate can directly probe the subband structure [8] as shown in Fig. 2. The inverse capacitance C_{tot}^{-1} is the proportionality constant between the change in the electrochemical potential and the amount of charge added to the nanotube, and consists of both an electrostatic term, C_{elec}, and a "quantum" or density-of-states term:

$$C_{tot}^{-1} = C_{elec}^{-1} + [e^2 g(E)]^{-1} . \tag{4}$$

The observed gate-voltage dependence of the capacitance in Fig. 2a results from the density-of-states given in (2) manifesting itself in the capacitance via (4). In the figure, the bandgap is clearly visible as a large dip in the measured capacitance, followed by features that correspond to the first and second 1D electron and hole subbands. Fitting (2) and (4) to the experimental data gives the electrostatic capacitance and bandgap of the nanotube, which are in good agreement with calculated values based on the device geometry and the tube diameter.

While the capacitance shows clear electron–hole symmetry around the bandgap, the conductance measured on the same device (Fig. 2b) does not. This reflects the fact that the capacitance depends only on the thermodynamic density of states while the conductance depends also on the carriers' scattering rates and the contact resistances. Thus, the capacitance gives us a clear picture of the nanotube band structure and the amount of charge carriers present at a given gate voltage. Transport, on the other hand, measures the transmission of electrons through the device, as discussed below.

1.2 1D Transport in Nanotubes

To fully understand the transport characteristics of carbon nanotubes, we start with the Landauer formula, which states that the conductance of a quasi-1D system is given by:

$$G = \frac{4e^2}{h} \sum_i \int_{-\infty}^{\infty} \frac{\mathrm{d}f[(E - E_F)/k_B T]}{\mathrm{d}E} \Im_i(E)\, \mathrm{d}E , \tag{5}$$

where $\Im_i(E_F)$ is the transmission of the ith 1D subband state at the Fermi energy and $\mathrm{d}f/\mathrm{d}E$ is the energy derivative of the Fermi function. Conductance is thus a measure of the transmission of electrons through the entire device at the Fermi energy, broadened by the finite thermal width of the Fermi function.

When the Fermi energy is in the bandgap, $\Im_i(E_F) = 0$ and the conductance is governed by thermal activation from the tails of the Fermi function. When E_F lies within an electron or hole subband, the transmission properties

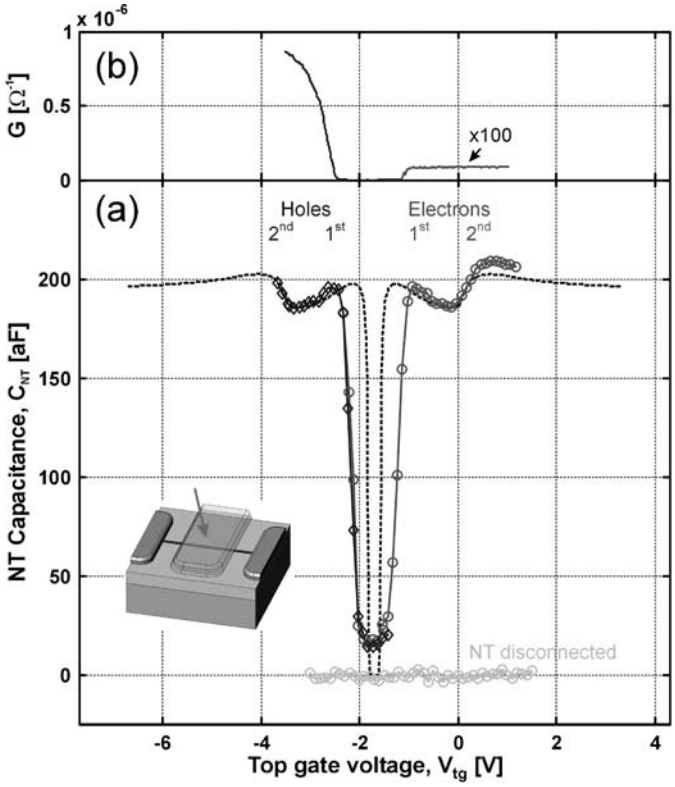

Fig. 2. Density dependence of the capacitance of a single SWNT. (**a**) Measured capacitance between an individual semiconducting SWNT and a metallic top-gate separated by 10 nm of SiO_x (scheme is shown in the *inset*). The *top trace* shows the dependence of the capacitance on the top-gate voltage. The *bottom trace* is the reference capacitance measured with the nanotube disconnected. The *dashed line* is a fit to a theory that includes elctrostatic and density-of-states contributions to the capacitance (2) and (4). (**b**) The conductance, G, measured on the same device. Adapted from [8]

of the entire device – tube plus contacts – determine the conductance. If the transport is ballistic and the tube has perfect contacts, this equation predicts a quantized conductance of $4e^2/h$ associated with each 4-fold degenerate 1D subband. Metallic nanotubes very often approach this quantized conductance value even at room temperature [9, 10]. Semiconducting nanotube devices have come within 25 % of this theoretical limit at room temperature [10, 11] and to within a few per cent at low temperatures [10–12], as discussed further in Sect. 4.

Conductance less than the quantized value can arise from additional resistance due to either the contacts or the tube. At or near room temperature, these two resistive contributions add incoherently, and are discussed sepa-

rately in Sect. 2 below. At lower temperatures, coherence effects and the Coulomb blockade become important. This quantum regime is discussed in Sect. 4.

2 Classical (Incoherent) Transport in Nanotubes

If we neglect coherence effects, the total resistance $R = G^{-1}$ of a nanotube device with a uniform channel can be written as:

$$R = R_{\text{contacts}} + R_{\text{tube}}\,, \tag{6}$$

where the contact resistance obeys $R_{\text{contacts}} \geq h/4e^2$, and for a uniform tube with diffusive scattering:

$$R_{\text{tube}} = (h/4e^2)(L/\ell)\,, \tag{7}$$

where L is the tube length, ℓ is the electron mean-free path for momentum relaxation, and we assume $L \gg \ell$. The measured device properties thus reflect the incoherent addition of the resistance of the tube and the contacts. A variety of measurements have been used to sort out the relative importance of these contributions in a given device. For example, electric force microscopy can measure the potential drop along the tube under current bias [13–15], directly probing the relative contributions. Devices where the contacts dominate [16] and ones where the tube properties dominate [11, 15] have been studied, as discussed below.

2.1 Contacts to Nanotubes: Schottky Barriers

Two types of barriers can form at the metal/tube interface and increase the contact resistance beyond the ideal $h/4e^2$ value. The first is a barrier created by an imperfect interface between the contact metal and the nanotube. Its resistance is a function of the cleanliness of the interface and the overlap of the metal–nanotube electronic states. Au and Pd have proven to make the best contacts to nanotubes, with near-perfect transmission frequently obtained [11].

More fundamental is the Schottky barrier that can form at the interface of a metal and a semiconducting nanotube. The properties of the Schottky barrier will depend on the band alignment at the interface (Fig. 3a). In the absence of interface states believed to be a good approximation for the metal/tube interface [17], the heights of the Schottky barriers for hole and electron injection are given by the work function of the metal contacts, ϕ_{M}, the work function of the nanotube, ϕ_{NT}, and its energy gap, E_{g} (see Fig. 3a):

$$\phi^p_{\text{SB}} = \phi_{\text{NT}} + E_{\text{g}}/2 - \phi_{\text{M}}\,, \qquad \phi^n_{\text{SB}} = \phi_{\text{M}} - \phi_{\text{NT}} + E_{\text{g}}/2\,. \tag{8}$$

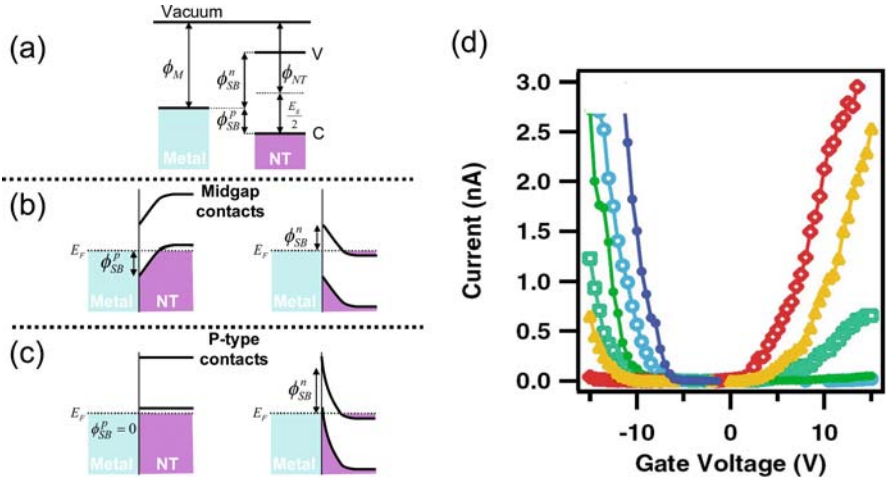

Fig. 3. Schottky-barrier height at the metal/nanotube interface. (**a**) A schematic of the nonaligned metal and nanotube energy levels depicting the relation between the Schottky-barrier heights for hole (/electron) injection, ϕ^p_{SB} (ϕ^n_{SB}) and the work-function of the metal, ϕ_{M}, the work function of the tube, ϕ_{NT}, and its energy gap E_{g}. When both are put in contact, band bending at the interface occurs to compensate for the work-function difference. (**b**) The case for contacts with the work function at the nanotube midgap. (**c**) p-type contacts. (**d**) Tuning the Schottky barrier from n- to p-type contacts using O_2. The *red curve* is the measured I–V with no exposure to oxygen. The remaining curves in order of increasing exposure to O_2 are colored *orange*, *light* and *dark green*, *light* and *dark blue*. Adapted from [16]

When the Fermi level of the metal lies at the midgap of the nanotube (Fig. 3b) there will be a Schottky barrier for both n and p carrier injection, whereas when it aligns with the hole band (Fig. 3c) there would be no barrier to hole injection but a large barrier to electron injection. This case corresponds to the semiconductor device in Fig. 2, where the on-state resistance in the n-regime far exceeds that of the p-regime. Thus, while the nanotube bands are electron–hole symmetric near the Dirac point, the contact properties generally are not.

A series of experiments, primarily by the IBM and Stanford groups, clarified the importance of Schottky barriers in SWNT transistors. Figure 3d shows measurements where the work function of the contact metal was adjusted for the same device by the adsorption of oxygen [16]. The device started out with predominantly n-type conduction, but as adsorbed oxygen increased the work function, the contacts changed to ambipolar, and finally to p-type. Other experiments on many different contact metals [11, 16, 18, 19] support this basic picture: high work function metals like Pd or Rh make good p-type contacts to tubes, while low work function metals like Al yield better n-type contacts. In all cases, adsorbed dipoles can strongly shift the metal work

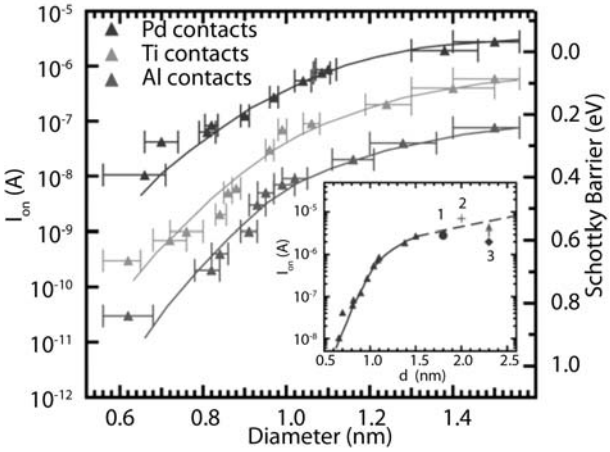

Fig. 4. On-state current and Schottky-barrier height as a function of SWNT diameter and contact metal. *Curves* from *top* to *bottom* correspond to Pd, Ti and Al. The right axis is the Schottky barrier, extracted from I_{on} using a self-consistent Poisson–Schrödinger model of the band bending near the contacts. *Inset* includes data points for Pd-contacted nanotube FETs from other publications. Adapted from [19]

functions, thus making the contact properties very sensitive to the ambient environment and device history. It was also noted [11] that a high work function by itself is not sufficient to assure ohmic contacts. For example, Pt has a larger work function than Pd but forms more resistive contacts, probably due to additional tunneling barriers formed as a result of poor wetting of the tube by the contact metal.

Since the energy gap grows with decreasing diameter ($E_g \sim 1/d_t$) it is clear from (8) that for every metal there exists a critical nanotube diameter below which a Schottky barrier with finite height will form and the height of this barrier will increase with decreasing diameter. Figure 4 shows the measured on-state current in the p-regime for nanotube transistors of different diameters and contact metals, along with the inferred Schottky barrier height. This height is seen to systematically grow with decreasing diameter. Ohmic p-type contacts are obtained only with Pd contacts to tubes of diameters > 1.5 nm.

These measurements provide a consistent picture of contact properties of semiconducting nanotubes. A major remaining challenge is to make good ohmic contacts to tubes with diameters 1.5 nm and smaller. Surprisingly, even small-bandgap/metallic tubes show significant barriers in this range [20]. The origin of this behavior is still not understood.

2.2 The Effect of Disorder

With an understanding of the role of contacts on nanotube conductance, we turn to examine the scattering properties of the nanotube channel itself and start by considering the effect of disorder. The major sources of disorder in nanotubes are:

Localized lattice defects, such as vacancies, substitutions, pentagon-heptagon defects and heterojunctions between nanotubes of different chiralities. Such defects are typically formed during nanotube growth, by volatile processing, or by intentional damage [21]. The atomically sharp nature of these defects leads to large momentum scattering.

Electrostatic potential fluctuations, created by a random distribution of charges in the substrate, by molecules adsorbed on the nanotube or by processing residues. These can induce both short- and long-range disorder.

Mechanical deformations, these include local strains and twists, which affect the local bandgap [22] as well as kinks that act as conductance barriers [23].

The coexistence of multiple sources of disorder in nanotube devices as well as the large variability in their properties makes it hard to make wide generalizations on the effects of disorder. Nevertheless, some understanding has emerged.

Experimentally, the effect of disorder is determined by extracting the nanotube corresponding mean-free paths from the conductivity (7) or by direct spatial imaging. Nanotubes with strong disorder show marked effects already at room temperature, whereas in cleaner nanotubes, disorder becomes the dominant scattering mechanism only at low temperatures. Low-temperature measurements of metallic tubes routinely show mean-free paths that are many micrometers long, as determined from their conductance [3, 24], from measured sizes of quantum dots [2, 3] and from scanned probe measurements [13, 25]. Semiconducting tubes, often show stronger sensitivity to disorder and shorter mean-free paths [4, 5]. However, they have also clearly demonstrated μm-long mean-free paths at low temperatures [26–30].

Disorder affects the transport in nanotubes in two distinct ways depending on its spatial scale, owing to two distinct backscattering processes – nanotubes have two degenerate dispersion branches originating from the K and K' points, each has left- and right-moving electrons. Backscattering can be either between the two branches or within the same branch. The first involves large momentum transfer, comparable to the inverse lattice constant and therefore occurs only from atomically sharp disorder. The latter requires small momentum transfer and is therefore caused by long-range disorder. It was further shown [31, 32], that due to the symmetries of the electronic wavefunctions, metallic tubes are affected only by short-range disorder, whereas

semiconducting tubes are affected by both short- and long-range disorder (see also contributions by Ando and by Spataru et al. in this book).

Scattering off atomic defects has been extensively studied theoretically [33–41], but the experimental situation is less clear. While localized scattering centers have certainly been observed in experiments [42–44], to date it has not been possible to probe the atomic-scale nature of the defect and to correlate it unambiguously with the observed transport properties.

Long-range disorder, e.g., from the electrostatic/mechanical interaction of a nanotube with the substrate is also known to be important, especially at low carrier densities in semiconducting nanotubes. The potential fluctuations break up the tube into a series of electronic puddles, with transport dominated by hopping between the puddles [45], as determined by a number of scanned probe measurements [13,14,25,46]. One manifestation of this is seen in the data of Fig. 2: The experimentally measured conductance and capacitance drop to zero well before the theoretical band edge is reached. At low carrier densities, the nanotube stops conducting before it runs out of carriers, as they become localized by a disorder potential along the nanotube length. We note that suspended nanotubes have shown dramatically improved transport characteristics, confirming this viewpoint, and allowing one to observe the first few electrons/holes added to a single-nanotube quantum dot. These will be discussed in Sect. 4.

2.3 Electron–Phonon Scattering in Nanotubes

In clean, high-quality metallic SWNTs at room temperature, the dominant scattering mechanism is well known to be electron–phonon scattering. Scattering by acoustic phonons dominates the resistances at small source–drain biases [47–49], whereas scattering by optical and zone-boundary phonons sets a limit on the maximal current carried by individual SWNT at large bias [49–51]. The latter is shown in Fig. 5 for a metallic nanotube. The slope of the current–voltage characteristic decreases for increasing bias, and, if the tube is suspended, can even become negative. This dramatic increase in resistance and saturation of the current at high electron energies was first explained by *Yao* et al. [50]: the electron rapidly emits a phonon as soon as it has an excess energy equal to the optical-phonon energy, $\hbar\omega_0 \sim 160\,\mathrm{meV}$. Recent experiments [49,51] have measured the phonon emission rate directly and confirm it to be very fast ($< 0.1\,\mathrm{ps}$). This emission process limits the current in all but the shortest nanotubes to currents less than $I_{\max} \sim (4e^2/h)(\hbar\omega_0/e) \sim 25\,\mu\mathrm{A}$. Metallic devices with short channels ($L \sim 10$–$15\,\mathrm{nm}$) comparable to the optical-phonon mean-free path [49, 51] ($l_{\mathrm{op}} \approx 10\,\mathrm{nm}$) have demonstrated sustained currents up to $110\,\mu\mathrm{A}$ in the high-field regime ($V_{\mathrm{SD}} \sim 1.5\,\mathrm{V}$) at room temperature [52].

The excess energy created by this phonon emission can be substantial, heating the tube significantly, particularly for suspended tubes. The phonons created can scatter additional electrons increasing the resistance even further.

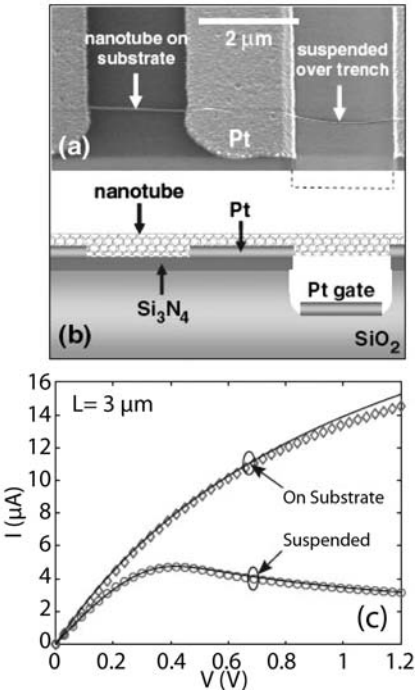

Fig. 5. Suspended tube I–Vs demonstrating the effect of optical-phonon scattering. (**a**) SEM image, taken at a 45° angle, of the nonsuspended (on nitride) and suspended (over a $\sim 0.5\,\mu$m deep trench) segments of the tube. (**b**) A schematic of the device cross section. (**c**) Current–voltage (I–V) characteristics of the same-length ($L \sim 3\,\mu$m) suspended and nonsuspended portions of a SWNT ($d_t \sim 2.4\,$nm) at room temperature measured in vacuum. The *symbols* represent experimental data; the *lines* are calculations based on average tube temperature (similar within $\sim 5\,\%$ to that based on actual tube-temperature profile and resistance integrated over the $\sim 3\,\mu$m tube length). Adapted from [53]

For suspended tubes, this effect is so strong as to lead to negative differential resistance [53] (Fig. 5), and the observed characteristics are in good agreement with a model [53] that accounts for the heat flow along the nanotube. The temperature can rise up to $\sim$ 1000 K, even creating significant light emission [54].

Recent measurements have shown that phonon scattering also limits the ultimate performance of semiconducting nanotube devices. Figure 6 shows the temperature dependence of the linear conductance of a clean nanotube device with good contacts [30]. The on-state resistance grows linearly with temperature, indicative of scattering by acoustic phonons, whose occupation also grows linearly with temperature; the mobility $\mu = (L^2/C_\mathrm{G})\,\mathrm{d}G/\,\mathrm{d}V_\mathrm{G}$ behaves in a similar way. Measurements on many semiconducting devices

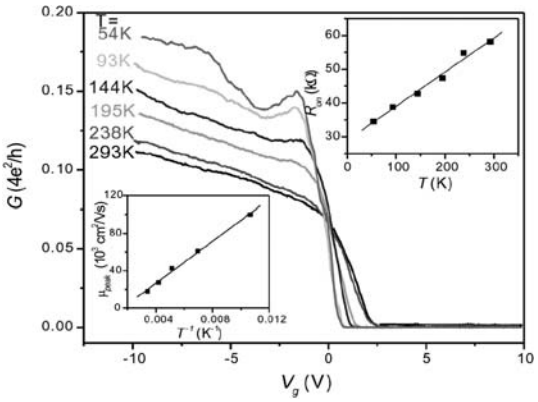

Fig. 6. Conductance and mobility of a p-type semiconducting nanotube transistor vs. temperature. *Main figure:* The conductance vs. gate voltage at different temperatures for a device with diameter $d_t = 4\,\text{nm}$ and length $L = 4\,\mu\text{m}$. *Upper inset:* R_{on} as a function of T. *Lower inset:* measured peak mobility as a function of T^{-1}. Both are shown with linear fitting. Adapted from [30]

yield the following approximate expression for the on-state mean-free path and the mobility:

$$l_{ap}(\text{on}) \approx 0.3\,\mu\text{m}\ \ d_t(\text{nm})\ \ \frac{300\,\text{K}}{T}\,,$$
$$\mu_{ap}(\text{max}) \approx 1000\frac{\text{cm}^2}{\text{Vs}}\ \ (d_t(\text{nm}))^2\ \ \frac{300\,\text{K}}{T}\,. \tag{9}$$

The peak mobility depends quadratically on the diameter of the nanotube, in agreement with theoretical predictions [55–57]. This dependence results from a decrease of both the effective mass and the scattering rate with increasing diameter.

The mobilities of clean semiconducting tubes are very high [26–30]. For the device in Fig. 6 $\mu_{peak} \sim 15\,000\,\text{cm}^2/\text{Vs}$ at room temperature, growing to $> 100\,000\,\text{cm}^2/\text{Vs}$ at $T = 50\,\text{K}$. These mobilities far surpass those found in silicon MOSFETs, fueling interest in nanotube transistor devices. This is discussed in the following section.

3 Nanotube Devices and Advanced Geometries

The high mobilities, long mean-free paths, and large current-carrying capacities of nanotubes have inspired many groups to explore a broad spectrum of electronic, high-frequency, optoelectronic, and nanomechanical applications of nanotubes as discussed also in the contribution by Endo et al. In this section we describe representative examples.

3.1 High-Performance Transistors

Since the first nanotube transistors were reported [4, 5], researchers have worked steadily to improve device performance through innovations such as improved contacts, shorter channels, and high-κ/thin dielectrics for improved gating, where κ refers to the dielectric constant. Figure 7 shows the I–V_{SD} characteristics of a nanotube transistor created using the high-κ dielectric, ZrO_2, and a top-gate electrode [58]. The I–V curves resemble those of a standard MOSFET, but show dramatically improved performance relative to Si or to previous backgated nanotube devices. The transconductance $\mathrm{d}I/\mathrm{d}V_G$ in the saturation regime of the transistor is $\sim 10\,\mu S$ at $V_{SD} = 1.2\,V$, and experiments on 50-nm channel length devices have achieved $30\,\mu S$ [59]. Normalized to the width of the tube, these transconductances are significantly larger than those obtained in Si MOSFETs. Furthermore, there is still room to improve: the theoretical limit, when the capacitance is governed by the quantum capacitance and the tube is in the ballistic-transport regime, is: $\mathrm{d}I/\mathrm{d}V_G = 4e^2/h \sim 155\,\mu S$.

Top-gated devices have also shown dramatic improvements in device subthreshold swing, $S = \ln(10)[\mathrm{d}V_G/\mathrm{d}\ln(I_{SD})]$, a key parameter in evaluating transistor performance that indicates how effectively the device turns off with gate voltage. Backgated nanotube transistors exhibited values of $S \sim 1$–$2\,V$/decade indicating a slow turn-off with V_G. This value should be compared with the theoretical limit of $k_B T \ln(10) = 60\,mV$/decade at room temperature, arising from thermal smearing of the Fermi distribution of carriers in the device. In contrast, top-gated nanotube transistors with thin or high-κ dielectrics routinely yield [58–61] $S \sim 70$–$130\,mV$/decade.

A final key device property is the ratio between the current through the transistor in its "on" state and the leakage current in the "off" state (the on/off ratio). Values in the range $\sim 10^6$–10^3 are common. Since, for an ambipolar device, this ratio depends exponentially on the bandgap [$\sim \exp(-E_g/2k_B T)$] smaller-diameter tubes give larger on/off ratios. However, smaller-diameter tubes have lower mobilities and are more prone to Schottky barrier effects, as discussed above. There is therefore a tradeoff between on/off ratio and the on-state current of the transistor.

The integration of multiple nanotube transistors into simple circuits has also begun. Perhaps the most sophisticated device yet created is shown in Fig. 8, where multiple transistors were created on the same long nanotube and connected into a ring-oscillator circuit, where transistors connected in a ring topology turn each other on/off sequentially in a looping domino effect [62]. The circuit oscillated at 50 MHz, limited not by the intrinsic performance of the nanotube transistors, but rather by the interconnect parasitics. The ultimate limits on frequency, device performance and circuit complexity remain to be explored, and are an active area of research, as discussed in the next section.

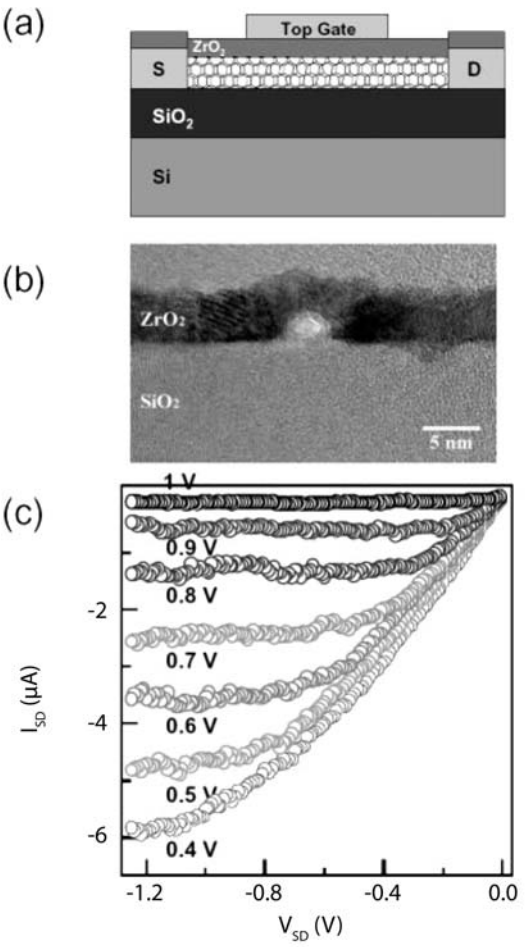

Fig. 7. High-κ nanotube transistor. (**a**) Sideview schematics of a SWNT-FET with ALD-ZrO_2 as the gate dielectrics (S and D represent the source and drain electrodes). The nominal thickness of ZrO_2 used is 8 nm. (**b**) TEM image of the cross section of a SWNT on SiO_2 with conformal coating of 4-nm thick ZrO_2. The circular region at the ZrO_2/SiO_2 interface is the cross section of a nanotube that exhibits light contrast in the TEM. (**c**) I–V curves of the FET recorded for various top-gate voltages. Adapted from [58]

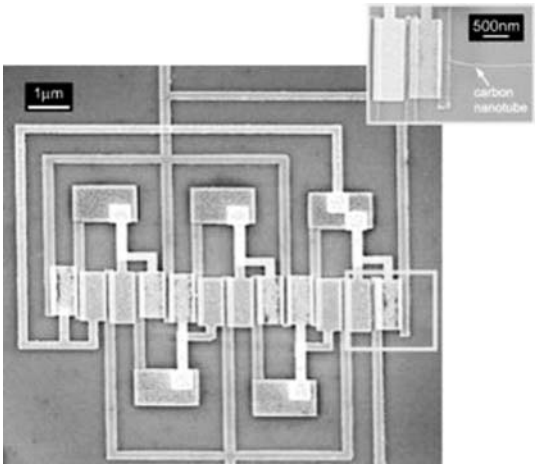

Fig. 8. An SEM image of a SWNT ring oscillator consisting of five CMOS inverter stages. Adapted from [62]

3.2 Radio-Frequency and Microwave Devices

In principle, nanotube transistors may operate up to the terahertz regime, but measurements of the high-frequency properties are difficult. The relatively high input impedance of a nanotube device ($R > h/4e^2 = 6.5\,\mathrm{k}\Omega$) limits device coupling efficiency into $50\,\Omega$ transmission lines, and this has served as a major impediment to device testing at RF/microwave frequencies. Nevertheless, a number of approaches have met with success. The most straightforward are measurements of the S-matrix, which characterizes the high-frequency transmission and reflection of a nanotube device. Changes in the nanotube impedance result in very small but measurable changes in the transmission/reflection coefficients. Both the resistive [63] and kinetic inductive portions [64] of a metallic nanotube impedance have been inferred. A measurement of a semiconducting tube in an FET geometry demonstrated a differential conductance at 1 GHz nearly identical to that at dc, indicating the potential for efficient operation at microwave frequencies [65].

Another approach is to use standard RF impedance-matching techniques to couple effectively to the nanotube. Several nanotube experiments have recently used the parasitic capacitance of the nanotube device itself in series or parallel with an external inductance in order to form a resonant circuit at $\omega_0 = 1/\sqrt{LC}$ with characteristic impedance matched to a 50-Ω transmission line [66, 67]. Variations in device resistance are mapped to modulation of the resonant circuit Q-factor, and hence to changes in the reflection or transmission of radiation at an applied carrier frequency (tuned to the circuit resonance). These techniques have been used to examine both transistor behavior and single-charge dynamics on microsecond timescales.

A third approach uses the nanotube transistor itself as the high-frequency signal detector. A transistor is a nonlinear device element since the conductance is a function of the applied gate or source drain voltage. Accordingly, it will rectify high-frequency signals to produce a dc response, or "mix" two high-frequency signals to produce sum and difference frequencies. Rectification and mixing using nanotube transistors at frequencies up to 50 GHz have been demonstrated by a number of groups [68–71]. Similarly, microwave detection and heterodyne detection exploiting nonlinearity in the I–V response of metallic nanotubes have recently been reported [72].

An interesting application of nanotube mixing has been to detect the motion of a vibrating nanotube in an electromechanical resonator device [68, 73, 74], as shown in Fig. 9. Nanotubes have among the highest Young's modulus known (see the contribution by Yamamoto et al. in this book), and can easily be prepared in suspended geometries, thus making them ideal candidates for use as electromechanical resonators and switches. In this device, the nanotube transistor was used as an electromechanical mixer. The vibration of the nanotube with respect to the gate changes the conductance at the vibration frequency f_0. An ac voltage is applied to the source-drain at a nearby frequency $f = f_0 + \Delta f$, resulting in a low-frequency output at Δf proportional to the amplitude of the mechanical vibration. Furthermore, the vibration frequency f_0 could be broadly tuned by the application of a dc gate voltage V_{G}, as shown in the figure.

While these initial results indicate the promise of nanotubes for high-frequency electronics, this field is only just beginning. For traditional applications requiring matching to 50 Ω, reducing the impedance of the device is critical. Devices incorporating multiple nanotubes in oriented arrays [75] or randomly oriented mats [76] have been shown to provide many parallel conductance channels, and hence reduce the device impedance. Single-tube devices, on the other hand, are naturally matched to the high impedances of the nanoscale electronic world and may prove useful as local detectors to read out the high-frequency behavior of other nanoscale devices.

3.3 P–N Junction Devices

Bipolar nanotube devices, where both electron- and hole-doped regions are present in the same device, are garnering increasing attention both for electronic and optoelectronic applications (see also the contribution by Avouris et al.). An example of a p–n junction device [77] is shown in Fig. 10. Separate gates are used to dope adjacent sections of the tube p- and n-type, coupled by an intrinsic region. The I–V_{SD} curves for this device show excellent rectification characteristics, with an exponential turn-on in forward bias and a reverse-bias breakdown voltage in excess of 10 V. Thermal measurements [78] show that the on-state conductance is thermally activated, and the parameters of the junction, from the bandgap to the transmission prob-

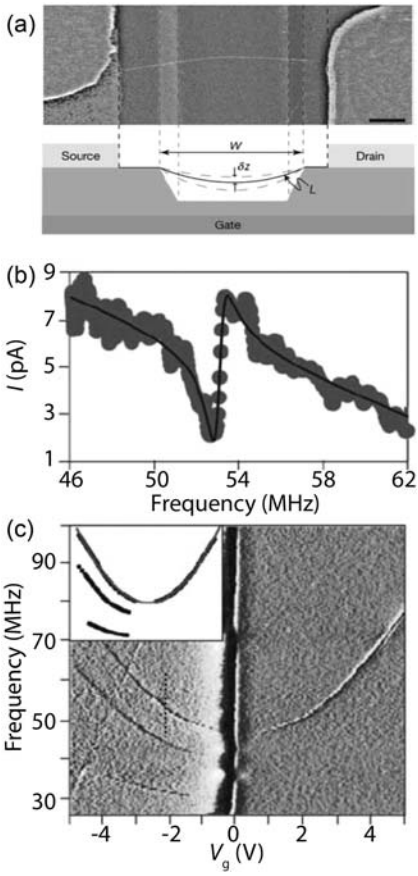

Fig. 9. Nanotube electromechanical resonantor. (**a**) An SEM image of a suspended device (*top*) and a schematic of device geometry (*bottom*). *Scale bar,* 300 nm. The sides of the trench, typically 1.2–1.5 μm wide and 500 nm deep, are marked with *dashed lines.* A suspended nanotube can be seen bridging the trench. (**b**) Detected current as a function of driving frequency. The *solid black line* is a Lorentzian fit to the data with an appropriate phase shift between the driving voltage and the oscillation of the tube. The fit yields the resonance frequency $f_0 = 55$ MHz, and quality factor $Q = 80$. (**c**) Detected current as a function of gate voltage V_G and frequency. The resonances in this figure are plotted as a function of gate voltage in the *inset.* Adapted from [68]

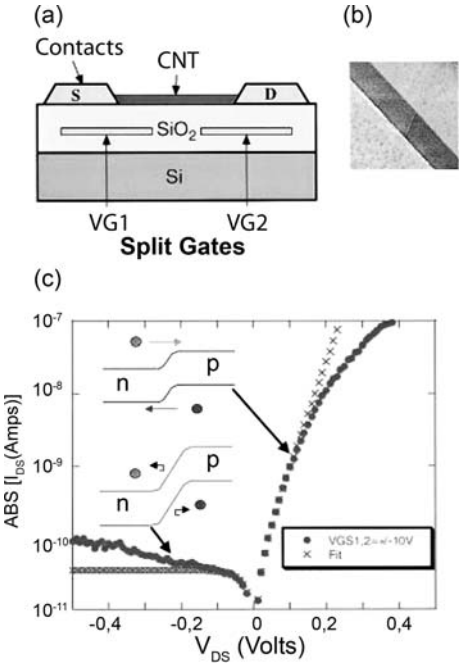

Fig. 10. Split-gate p–n junction device. (**a**) Schematic cross section of the device. The split gates V_{G1} and V_{G2} are used to electrostatically dope a SWNT. For example, a p–n junction with respect to the S contact can be formed by biasing $V_{g1} < 0$ and $V_{g2} > 0$. (**b**) SEM of a SWNT over a 1-μm split gate. (**c**) I–V curve plotted in absolute magnitude of the current. The band diagram illustrates the band structures during forward and reverse bias near the vicinity of the p–n junction. The fit is to the diode equation given with an ideality factor of $n = 1.2$ and $I_0 = 3 \times 10^{-11}$ A. Adapted from [77]

ability, can be inferred. Similar devices are proving to be ideal for studies of the photoconductivity in nanotubes.

p–n–p and n–p–n geometries are also easily created by separately gating different portions of the nanotube. To date, no one has demonstrated three-terminal bipolar transistor operation due to the difficulty of properly contacting the central or "base" region of the nanotube. Nevertheless, these devices have proven useful for a number of fundamental studies. One example [79] is shown in Fig. 11a, where a nanotube is partially suspended over a substrate. While the oxide-bound segments are p-doped by the substrate, the suspended section is intrinsic and thus forms a barrier for transport. A back-gate can offset the energy bands of the suspended section and as a result change the height of the transport barrier. Just before an n-type region is formed in the suspended segment (Fig. 11b), the height of the barrier is equal to the energy gap. Figure 11c shows thermal activation measurements across

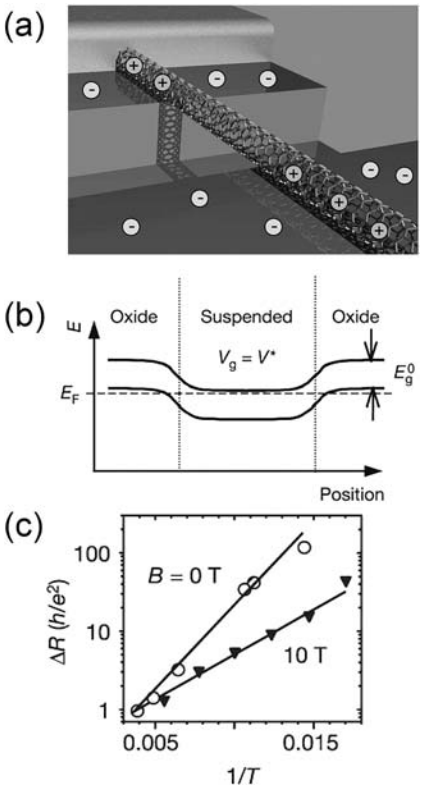

Fig. 11. p–n–p geometry for measuring bandgaps. (**a**) Schematics of a SWNT device partially suspended over a Si/SiO_2 substrate and contacted by source and drain electrodes (only one is shown). Charges on the substrate dope the oxide-bound segments p-type and a buried backgate is used to electrostatically dope the tube. For small positive gate voltages the suspended segment of the tube become n-type, while the oxide-bound segments remain p-type. (**b**) Energy-band diagram corresponding to a gate voltage just before an n-type region is formed in the suspended segment. At this gate voltage the number of thermally activated carriers is minimized, there is no n-type region to facilitate tunneling processes and the tube shows its highest resistance, $R_{\max}$. (**c**) Plot of the maximum resistance after subtracting the contact resistance $\Delta R = R_{\max} - R_{\text{contacts}}$ as a function of the inverse temperature for the nanotube in a magnetic field of 10 T and in zero magnetic field. Adapted from [79]

this barrier from which the bandgap can be directly deduced. These measurements demonstrate that the bandgap decreases linearly with magnetic field at a rate predicted by (3) above. The size of the inferred orbital magnetic moment is an order of magnitude larger than in atoms due to the large radius of the nanotube. Both the orbital and (smaller) spin magnetic moments will play important roles in the nanotube quantum dot measurements presented in the following sections.

4 Quantum Transport

At low temperature, a variety of quantum effects appear in transport in nanotubes. Because the energy scales for these quantum effects typically increase with decreasing system size, the "low-temperature" regime is often more readily reached in nanotubes than in other mesoscopic electronic devices, making nanotubes an attractive system to investigate basic quantum transport effects.

Quantum transport effects include the Coulomb blockade of conduction associated with charge quantization, interference effects associated with coherent wave properties of the charge carriers, periodic shell-filling signatures associated with resonant tunneling through orbital energy levels, Kondo effects associated with a spin degree of freedom on a confined nanotube hybridizing with the continuum of states in the metallic leads, and effects of ferromagnetism and superconductivity in the leads.

Effects of confinement and electron–electron interaction unique to one dimension, and associated with the separation of spin and charge degrees of freedom in excitations, can be identified in transport as power-law dependences of conduction on temperature and source–drain voltage.

Figure 12, showing differential conductance as a function of gate voltage and source–drain bias, provides an overview of various quantum transport regimes for a single tube connected to metallic leads, depending on the coupling of the tube to metallic leads. Evident are the crossovers from Coulomb-blockaded transport, to a fourfold shell-filling structure, to standing-wave (Fabry–Perot) resonances as the conduction between the nanotube and its metallic leads is altered by gross changes in backgate voltage [80].

4.1 Quantum Transport in One Dimension

4.1.1 Luttinger Liquid

In two and three spatial dimensions, the metallic state of interacting electrons is a Fermi liquid, with elementary excitations carrying charge e and spin 1/2, and behaving as weakly interaction fermions. In one dimension, interacting electrons cannot be described as Fermi liquids; spin and charge excitations are described as bosonic modes, are separable, and propagate at different velocities. The Fermi surface is not abrupt, even at zero temperature, and various power-law dependencies are expected in transport. This state is referred to as a Luttinger liquid [81,82]. Nanotubes are a nearly ideal realization of interacting electrons or holes in one dimension, and so provide an excellent testing ground for theoretical predictions of the behavior of Luttinger liquids, particularly in transport.

Power-law scaling of the conductance $G = \mathrm{d}I/\,\mathrm{d}V_{\mathrm{Sd}}$ with temperature T and source–drain bias V_{Sd}, distinctive features of transport through a Luttinger liquid, has been observed in nanotubes in several experiments [8, 42,

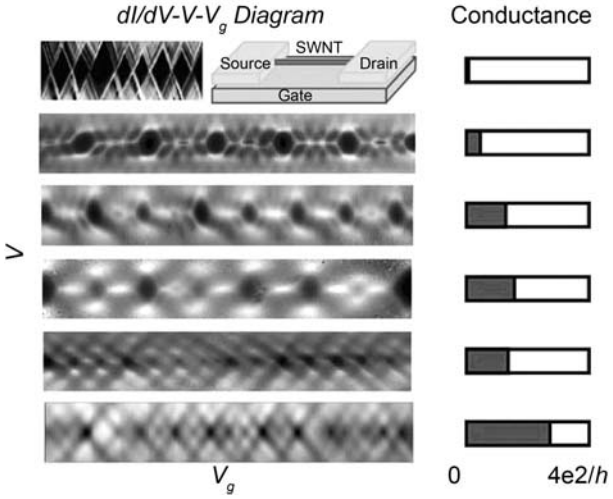

Fig. 12. As the tunnel barrier between nanotube and metallic leads goes from being highly reflecting (*top panels*) to being highly transmitting (*bottom*), the pattern of conductance (*gray scale*) as a function of gate voltage V_g and source–drain voltage V transforms from Coulomb-blockade diamonds, marking the addition of one charge to the nanotube dot per diamond (stripes in the conducting region reflect excited states of the dot) to a fourfold-degenerate pattern, marking the filling of degenerate manifolds (two spin states, two orbital states), to a one-dimensional standing-wave (Fabry–Perot) interference pattern in the nearly open (conductance $\sim 4e^2/h$) regime. *Upper right inside* shows device schematic. Adapted from [80]

83, 84]. For instance, *Bockrath* et al. [83] measured SWNTs contacted either from the top (effectively ending the tube at the contact) or from below (contacting the tube along its bulk), and in both cases find a power law $G(T) \propto T^{\alpha}$ for the zero-bias conductance, with α depending on the fabrication details ($\alpha_{\text{end}} \sim 0.6$, $\alpha_{\text{bulk}} \sim 0.3$) and a similar power law for the differential conductivity at finite bias, $\mathrm{d}I/\mathrm{d}V_{\text{SD}} \propto V_{\text{SD}}^{\alpha}$ yielding comparable values for α. The Luttinger parameter, g, which characterizes the strength and sign of the electron interaction, can be related to readily measured nanotube parameters E_{C}, the charging energy, and Δ the mean orbital level spacing by $g = (1 + 2E_{\text{C}}/\Delta)^{-1/2}$. Estimates and previous measurements give $E_{\text{C}}/\Delta \sim 6$ yielding a theoretical value $g \sim 0.28$, independent of tube length. For a SWNT with four conducting modes, theory also relates α to g: $\alpha_{\text{end}}(\text{theory}) \sim (g^{-1} - 1)/4$, $\alpha_{\text{bulk}}(\text{theory}) \sim (g^{-1} + g - 2)/8$, giving $\alpha_{\text{end}}(\text{theory}) \sim 0.65$ and $\alpha_{\text{bulk}}(\text{theory}) \sim 0.24$, in good agreement with experiment.

4.1.2 Ballistic Transport

Several experiments [11, 13, 51, 85–87] have demonstrated ballistic 1D transport in nanotubes, where the mean-free path of charge excitations exceeds the tube length. The four modes of a SWNT (two for spin, two for orbital degeneracy) give an expected intrinsic conductance of $4e^2/h \sim 6.5\,\mathrm{k}\Omega^{-1}$ for a ballistic nanotube, not including any additional extrinsic resistance at the contacts. Recent measurements on SWNTs with nearly ideal Pd contacts and local, gate-controlled depletion regions, show that the four 1D modes can be depleted one at a time, yielding quantized conductance plateaus [12] as a function of a gate voltage, as shown in Fig. 13. Surprisingly, even in zero applied magnetic field, the plateaus are spaced by e^2/h rather than the expected $2e^2/h$ for spin-degenerate states. The number and spacing of the plateaus, their energy spacing, and their evolution under applied source–drain bias [88] suggest that both orbital and spin degeneracy are lifted during the gate-depletion process. Similar effects have recently been observed in various semiconductor nanowire [89] and bulk heterostructure devices [90–92], and may also be related to the unexpected (but ubiquitious) appearance of an extra conductance plateau as a function of gate voltage, appearing much like a spin-split feature, though at zero magnetic field, at a conductance around $0.7(2e^2/h)$ in semiconductor quantum point contacts [93].

In ballistic nanotubes, conductance oscillations arising from 1D standing-wave-like quantum interference [9] of charge carriers are seen, comparable to Fabry–Perot oscillations in an optical cavity as a function of wavelength or cavity length. These are shown, as an example, in the bottom two panels of Fig. 12.

4.2 Superconducting Proximity Effect

When nanotubes are contacted with superconducting electrodes, signatures of proximity-effect superconductivity can appear [24, 94]. In a recent experiment [95], metallic carbon nanotubes were contacted with multilayer Ti/Al electrodes in a four-probe geometry in order to mitigate the effect of series contact resistance. Below a critical temperature, zero-resistance supercurrents are observed as long as the normal-state conductance is sufficiently high ($\sim 2e^2/h$), indicating highly transparent contacts.

Imperfect transmission at the interfaces produces broadened zero-dimensional (standing-wave) states in the energy-level structure. In normal-state devices, this leads to Fabry–Perot oscillations [9] as a function of gate voltage V_G as seen in the bottom panels of Fig. 12. In the case of the superconducting proximity effect, the broadened zero-dimensional states lead to periodic modulation of the critical current, I_C, as a function of V_G, as seen in Fig. 14. Finite-length Fabry–Perot effects, however, were not able to explain the magnitude of the fluctuations in I_C. Rather, Josephson dynamics indicating multiple reflections were demonstrated by correlating I_C with

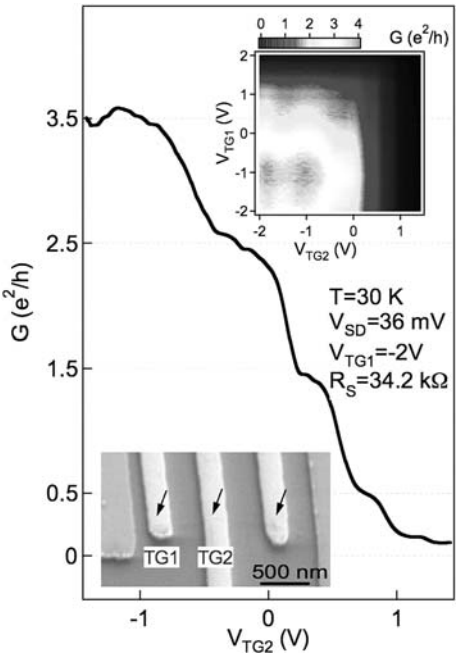

Fig. 13. Evidence of four-step conductance quantization in a single-wall nanotube with highly transparent Pd contacts, in units of the spin-resolved quantum of conductance, e^2/h, at the high-bias half-plateaus. No external magnetic field is applied: $B = 0$. Valley degeneracy can be broken by deformation of the tube, but where is spin degeneracy? *Lower inset* shows the device, with top gates passing over the tube. *Upper inset* shows conductance as a function of two top gates, demonstrating independent gating (*square gray scale pattern*) and a plateau structure for each gate. R_s is the extracted series resistance. Adapted from [12]

the normal-state conductance [95]. Additionally, the differential resistance, $\mathrm{d}V_{\mathrm{sd}}/\,\mathrm{d}I$, measured for current biases in excess of the gate-voltage-dependent $I_{\mathrm{C}}(V_{\mathrm{G}})$ shows modulation on the same voltage scale as that for I_{C}. Multiple Andreev reflections appear as peaks in $\mathrm{d}V_{\mathrm{sd}}/\,\mathrm{d}I$ as a function of applied current bias.

Following this work, more complex device geometries using the gate-tunable supercurrents in nanotubes have been realized. Nanotubes embedded in superconducting devices have been used as tunable Josephson junctions, displaying many of the dc and RF characteristics of standard junctions [96]. A recent experiment demonstrated the formation of a nanotube-based superconducting quantum interference device (SQUID) containing two carbon-nanotube sections connected to an Al loop [97].

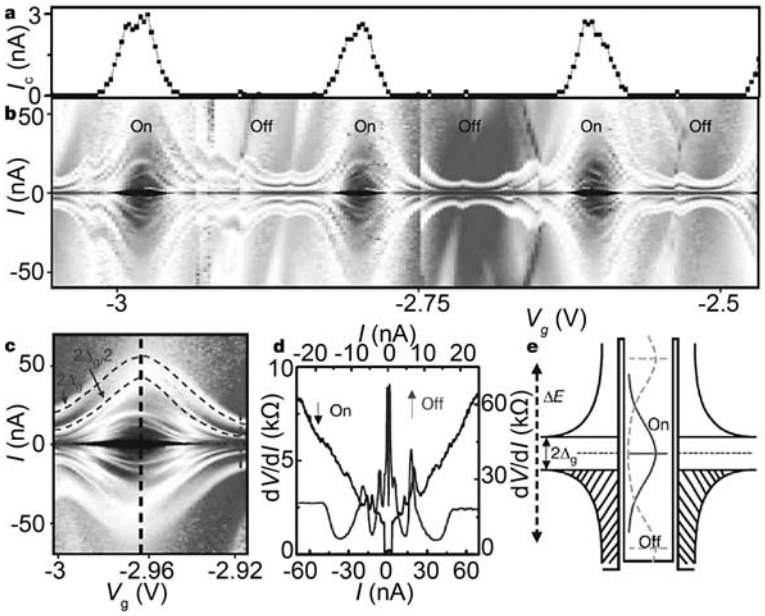

Fig. 14. (**a**) Dependence of critical current I_C on gate voltage, V_g. (**b**) Grayscale of dV/dI, with black representing zero. (**c**) High-resolution plot of dV/dI vs V_g, emphasizing multiple Andreev ridges. (**d**) Cuts through (**c**) at *dashed vertical lines*. (**e**) schematic energy-space diagram showing strongly coupled dot between superconducing leads. *Solid curve* in the central dot region shows "on" state; *dashed curve* shows off state. Adapted from [95]

4.3 Quantum Transport with Ferromagnetic Contacts

Experiments on multiwall carbon nanotubes with ferromagnetic contacts demonstrate the capability of nanotubes to sustain coherent spin transport [98–100]. This was observed through a modification of the device current dependent upon reversing the relative contact magnetizations, with antiparallel (AP) alignment typically producing higher device resistance than parallel (P), and hence a positive magnetoresistance, defined as $[(R_{AP} - R_P)/R_P]$.

Single-wall nanotubes contacted with highly transparent ferromagnetic PdNi leads display Fabry–Perot interference at 4.2 K [101, 102]. It was found that the magnetoresistance oscillated with the conductance, as shown in Fig. 15. These observations are well explained by a spin-dependent Landauer–Büttiker model [103] that independently accounts for the transmission probabilities of majority and minority carriers.

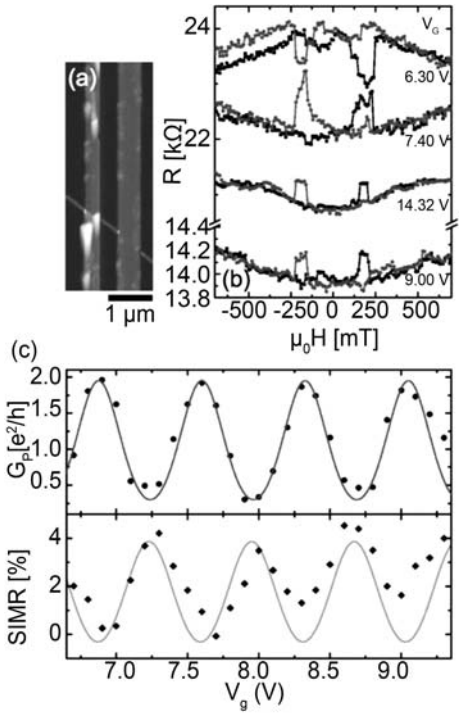

Fig. 15. (**a**) Atomic force micrograph of SWNT with asymmetric PdNi ferromagnetic leads, with the size scale indicated. (**b**) Two-terminal resistance traces as a function of applied magnetic field $\mu_0 H$. Usually, oppositely oriented magnetization leads to higher resistance. In some cases, it leads to a decrease in resistance (e.g., $V_g = 6.30\,\mathrm{V}$). (**c**) Comparison with experiment of theoretical predictions based on a spin-dependent Laudauer–Büttiker approach for calculating the gate-voltage-dependent conductance, and amplitude of spin-induced magnetoresistance (SIMR). Adapted from [101]

5 Nanotube Quantum Dots

A small conducting island – termed a quantum dot or a single-electron transistor – coupled via tunneling to the rest of a circuit, can show signatures of single-electron charging in transport at moderately low temperatures [104]. The requirement of tunneling implies contact resistances in excess of $h/e^2 \sim 26\,\mathrm{k}\Omega$. In addition, the energy required to add a single electron to the island, $e^2/2C$, where C is the island capacitance, must exceed the thermal energy $k_\mathrm{B}T$. Quantum confinement effects may also be observed as a discrete-level structure with orbital spacing Δ. Given the total capacitance values of the order of attofarads ($10^{-18}\,\mathrm{F}$) and energy scales E_C, Δ up to the meV range, single-electron charging effects are most commonly manifested at cryogenic temperatures $< 4\,\mathrm{K}$. Transport measurements are typically performed

as a function of source–drain bias V_{SD} across the island and gate voltage V_G, which shifts the energy levels of the dot. Such measurements permit a full mapping of discrete charge states (manifested as the Coulomb blockade), the excited-state energy spectrum, and exotic multibody interactions, since transport is allowed only when a single-particle energy level is aligned with the chemical potential of the leads [105].

5.1 Single Dots

Highly resistive contacts to carbon nanotubes have proved to be effective tunnel barriers for defining quantum dots. In such a geometry, the bulk of the nanotube forms the zero-dimensional island that is tunnel-coupled to metal leads. In a standard backgated configuration, the Si wafer serves as a gate electrode, which is capacitively coupled to the island [3].

In nanotube quantum dots, E_C is generally of the order of a few meV, and is set by the capacitance of the device. Approximating the capacitance per unit length from the formula for a coaxial cable $C/L = 2\pi\kappa\varepsilon_0 \ln(2h/r)$, where $\kappa \sim 2.5$ is the average of the dielectric constants of SiO_2 and vacuum, h the tube to backgate distance, and $r \sim 1\,\text{nm}$ the tube radius, we find a capacitance per unit length, $C/L \sim 19\,\text{aF}/\mu\text{m}$, and a charging energy, $E_C \sim 8\,\text{meV}/\mu\text{m}$, for a 1-μm gate oxide (a fairly standard value for thermally oxidized wafers).

The zero-dimensional energy-level spacing, Δ, may also be calculated for a carbon nanotube quantum dot of length L. In addition to the quantization of transverse momentum along the circumferential direction, the finite extent of a carbon-nanotube quantum dot leads to the quantization of momentum along the tube axis as $\Delta k = \pi/L$. Linearity of the bands near the Fermi level suggests that one may write

$$\Delta = \frac{h v_F \Delta k}{2 \times 2} \tag{10}$$

with Fermi velocity $v_F = 8.1 \times 10^5\,\text{m/s}$, which gives $\Delta \sim 0.4\,\text{meV}/\mu\text{m}$. The factors of two account for the band and spin degeneracy of the 1D subbands, and should be included when these degeneracies are lifted.

5.2 Band and Spin Effects in Single Quantum Dots

5.2.1 Shell Filling in Nanotube Dots

Transport in nanotube quantum dots shows the familiar characteristics of Coulomb blockade and bias spectroscopy down to individual electrons and holes. A number of experiments have demonstrated even–odd spin filling, where electrons are added to a single orbital level in pairs, occupying states of opposite spin. Experimentally [106] this filling scheme appears as an alternating large–small spacing between the narrow peaks of the conductance that

separate regions of Coulomb-blockaded transport, reflecting a corresponding alternation of addition energy between E_C and $E_C + \Delta$.

The interplay of spin and orbital degeneracies and the energetics of filling a 1D dot with interacting, spatially correlated electrons can lead to interesting filling patterns [107,108], as seen in the middle panels of Fig. 12. Experiments on clean isolated quantum dots, in both suspended and standard carbon nanotubes, show a fourfold periodicity in the addition energy spectrum [109], corresponding to the fourfold degeneracy of the nanotube levels [108, 110–112].

5.2.2 Nanotube Dots with Ferromagnetic Contacts

For experiments on nanotube quantum dots coupled to ferromagnetic leads, the relevant quantity to characterize coherent spin transport is the tunneling magnetoresistance (TMR), defined as TMR $= (R_{AP} - R_P)/R_P$ with subscripts AP and P denoting antiparallel and parallel contact magnetic moments, respectively. If spin transport can be modified *in situ*, it is possible to reverse the sign of the measured TMR. In transport experiments this is accomplished under the influence of an applied gate potential, producing a voltage-controlled spin valve.

Using single- and multiwall nanotube quantum dots contacted with NiPd [100] the Basel group demonstrated sign reversal of the TMR as a function of V_G [102, 113], comparable to the open-transport data [95] in Fig. 15. For SWNT devices the TMR signal oscillates with the same period as the Coulomb-blockade features in transport. The oscillation period, lineshape, and inversion magnitude of the TMR signal are consistent with a model of spin-dependent transmission through localized states on the nanotube dot.

5.3 Kondo Effects in Nanotube Dots

The Kondo effect arises from the hybridization of a localized spin (or any degeneracy within a localized system that can serve as a two-level system) with a continuum of conduction electrons below a characteristic temperature, T_K [114]. When the leads of a two-terminal device are the continua with which the localized spin hybridizes, characteristic transport features appear [115]. These can be readily understood as reflecting a density of states (for the hybridized state) within the dot at the Fermi energy of the lead participating in the hybridization. The Kondo effect in nanotubes was first investigated in 2000 by *Nygard* et al. [116] and shows all of the familiar Kondo-transport features, along with some unique to nanotubes, such as fourfold shell filling [116]. Novel Kondo-related phenomena have appeared in carbon nanotubes owing to both their unique band structure and the ability to produce nanotube quantum dots with non-Fermi liquid leads (e.g., superconducting leads). We highlight a few recent results in the following subsections.

5.3.1 Nonequilibrium Singlet–Triplet Kondo Effect

The Kondo effect is generally observed as a conductance peak at zero bias that appears for $T < T_K$ when the dot is occupied by an odd number of electrons. It was recently shown [117] that the lifted degeneracy between the singlet (spin = 0) and triplet (spin = 1) configurations of a nanotube dot occupied by an *even* number of electrons – somewhat similar to a spin 1/2 system in a magnetic field, though at zero field the triplet is threefold degenerate – also is described by a Kondo effect that appears at a finite source–drain bias V, corresponding to an energy splitting of singlet and triplet energies. In this case, applying an external magnetic field lifts the degeneracy of the triplet state, splitting the single peak in the differential conductance at finite bias into three distinct finite-bias peaks, separated in bias voltage by $\Delta V = g\mu_B B/e$. The splitting provides a straightforward measurement of the electron g factor, which is found to be $g \sim 2$. It was also found that the narrow conduction peaks at finite bias could only be modeled theoretically using a full Kondo treatment.

5.3.2 Orbital and SU(4) Kondo

Kondo correlations can also arise when an orbital degree of freedom serves as the localized two-level system. Since carbon nanotubes possess both band and spin degeneracies, it becomes possible to realize a higher-order Kondo system comprising both spin and orbital degrees of freedom. This system is described by a four-component vector and accordingly an SU(4) symmetry group.

The orbital Kondo effect was realized experimentally [110] in a nanotube quantum dot with an applied field parallel to the tube axis. This field couples to the magnetic moments of the clockwise and counterclockwise circulating electrons (the two isospin states) and tunes the degeneracy between isospin levels. Kondo ridges with appropriate temperature dependences appear at finite values of parallel field in the Coulomb valleys.

The full SU(4) Kondo symmetry appears at zero magnetic field in a regime of gate voltage that displays fourfold symmetry [110]. In Coulomb valleys with unpaired spins, an unusually strong Kondo enhancement is apparent at zero bias, consistent with theory (Fig. 16). As a function of applied magnetic field and source–drain voltage, the Kondo SU(4) resonance splits into four components.

An interesting interplay [118] between the Kondo effect and multiple Andreev reflections (MAR) was investigated in nanotube quantum dots with strong tunnel coupling to superconducting Au/Al leads [119]. This device satisfies the criterion for observing MAR: $E_C \leq \Gamma \sim \Delta_G \leq \Delta$, where E_C is the charging energy, Γ the level broadening due to coupling to the leads, Δ_G is half the superconducting gap of the leads and Δ the mean level spacing of the dot. These processes appear as transport resonances when the

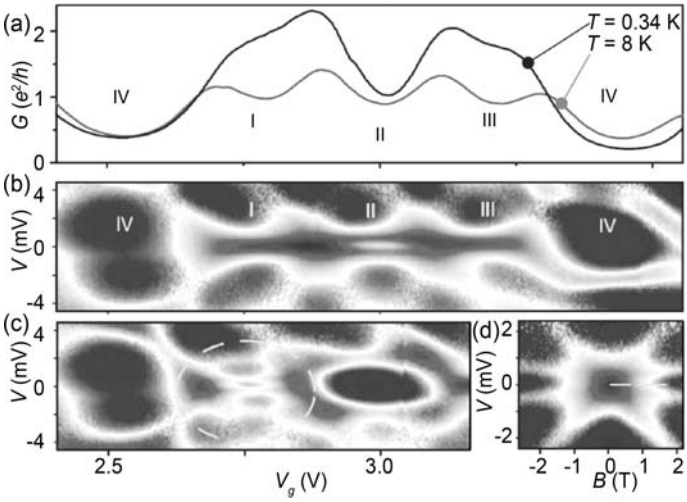

Fig. 16. (**a**) Conductance G as a function of backgate voltage V_g at 8 K and 0.34 K. Signature of the Kondo effect in valleys I and III is the rising conductance at decreased temperature. (**b**) Conductance (grayscale) as a function of V_g and source–drain voltage V at 0.24 K and $B = 0$. (**c**) Same as (**b**) except at 1.5 T. *Circle* marks fourfold splitting region. (**d**) Fourfold splitting of the Kondo peak as a function of field. Adapted from [110]

source–drain bias satisfies $V_{sd} = 2\Delta_G/ne$, with n an integer. Subsequent experiments demonstrating asymmetric device structures with one normal and one superconducting lead have also been performed in the presence of Kondo correlations [120].

5.4 Multiple Quantum Dots

The standard nanotube quantum dot device geometry, with two contacting leads and a single backgate, is ideal for making single quantum dots, but is not well suited for multidot structures since each dot usually requires independent control of tunneling and electrostatics in order to make interesting devices.

Experimental demonstrations of electrostatic depletion regions [12, 121] in a nanotube formed by the application of a voltage to a narrow topgate electrode were reported in [12, 121]. Based on this method, multidot structures were defined by several depletion gates on a single nanotube with transparent Pd electrodes [122]. A series of barrier gates produced local depletion regions in the tube, which served as tunable tunnel barriers, while plunger gates were used to shift the energy levels of the dots formed between the barrier gates (Fig. 17a). Double quantum dots produced in this way are fully tunable, as shown in Fig. 17. Several groups produced devices in similar configurations with comparable behavior [123–125]. Transport measurements on these tunable double quantum dots have now demonstrated signatures of fourfold

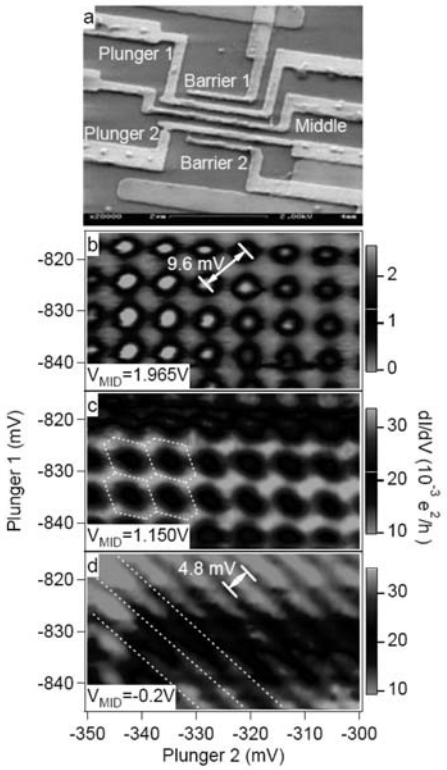

Fig. 17. (**a**) Electron micrograph of top-gated double quantum dot device. Barrier gates define the dots, plunger gates tune the electrostatics of the dots. (**b**) Square array pattern of Coulomb-blockade peaks in the conductance (*grayscale*) as a function of two plunger-gate voltages in the regime of small tunnel coupling and capacitive coupling of the two dots. Each peak marks a transition in the electron number of both of the dots. (**c**) As the middle gate separating the dots becomes less positive, tunneling of holes between the two dots as well as dot–dot crosscapacitance is increased, resulting in a hexagonal pattern of Coulomb-blockade conductance peaks. (**d**) At still lower gate voltage, the two dots merge, and the Coulomb-blockade pattern appears as a series of diagonal bands, where one plunger gate compensates the other, acting on the same large single dot. Adapted from [122]

shell filling in both the honeycomb charge-stability diagram and finite-bias triangles [123].

6 Future Directions

This chapter has presented an overview of the most significant advances in nanotube transport measurements over the past several years. We expect

that transport measurements on nanotubes will continue to produce fruitful experimental studies of basic physical phenomena.

We anticipate that hybrid devices [67], incorporating nanotubes and other nanoelectronics elements will become more common. We also anticipate that the weak hyperfine coupling [126] in carbon will make nanotubes a material system of choice for spin-based quantum information systems.

We anticipate high-frequency phenomena [70, 127] such as quantized vibrational modes or plasmons to become more widely investigated as techniques to measure nanotubes in the terahertz–far-infrared frequency regime are developed. We also expect that optoelectronic devices – structures where electrons and holes are converted to photons (or vice versa) – will open up new vistas for fundamental physics and device applications. While many of the basic transport phenomena in nanotubes are now understood, endless opportunities await the utilization of this unique system to explore the science of the nanoscale world.

References

[1] S. Iijima: Helical microtubules of graphitic carbon, Nature **354**, 56–58 (1991) 455

[2] S. J. Tans, M. H. Devoret, H. J. Dai, A. Thess, R. E. Smalley, L. J. Geerligs, C. Dekker: Individual single-wall carbon nanotubes as quantum wires, Nature **386**, 474–477 (1997) 455, 463

[3] M. Bockrath, D. H. Cobden, P. L. McEuen, N. G. Chopra, A. Zettl, A. Thess, R. E. Smalley: Single-electron transport in ropes of carbon nanotubes, Science **275**, 1922–1925 (1997) 455, 463, 480

[4] S. J. Tans, A. R, M. Verschueren, C. Dekker: Room-temperature transistor based on a single carbon nanotube, Nature **393**, 49–52 (1998) 455, 463, 467

[5] R. Martel, T. Schmidt, H. R. Shea, T. Hertel, P. Avouris: Single- and multi-wall carbon nanotube field-effect transistors, Appl. Phys. Lett. **73**, 2447–2449 (1998) 455, 463, 467

[6] S. G. Louie: in *Carbon Nanotubes* (Springer, Berlin, Heidelberg 2001) pp. 113–145 456

[7] Z. Yao, C. Dekker, P. Avouris: in *Carbon Nanotubes* (Springer, Berlin, Heidelberg 2001) pp. 147–171 456

[8] S. Ilani, L. A. K. Donev, M. Kindermann, P. L. McEuen: Measurement of the quantum capacitance of interacting electrons in carbon nanotubes, Nature Phys. **2**, 687–691 (2006) 458, 459, 474

[9] W. J. Liang, M. Bockrath, D. Bozovic, J. H. Hafner, M. Tinkham, H. Park: Fabry–Perot interference in a nanotube electron waveguide, Nature **411**, 665–669 (2001) 459, 476

[10] J. Kong, E. Yenilmez, T. W. Tombler, W. Kim, H. J. Dai, R. B. Laughlin, L. Liu, C. S. Jayanthi, S. Y. Wu: Quantum interference and ballistic transmission in nanotube electron waveguides, Phys. Rev. Lett. **87**, 106801 (2001) 459

[11] A. Javey, J. Guo, Q. Wang, M. Lundstrom, H. J. Dai: Ballistic carbon nanotube field-effect transistors, Nature **424**, 654–657 (2003) 459, 460, 461, 462, 476
[12] M. J. Biercuk, N. Mason, J. Martin, A. Yacoby, C. M. Marcus: Anomalous conductance quantization in carbon nanotubes, Phys. Rev. Lett. **94**, 026801 (2005) 459, 476, 477, 483
[13] A. Bachtold, M. S. Fuhrer, S. Plyasunov, M. Forero, E. H. Anderson, A. Zettl, P. L. McEuen: Scanned probe microscopy of electronic transport in carbon nanotubes, Phys. Rev. Lett. **84**, 6082–6085 (2000) 460, 463, 464, 476
[14] S. J. Tans, C. Dekker: Molecular transistors – potential modulations along carbon nanotubes, Nature **404**, 834–835 (2000) 460, 464
[15] Y. Yaish, J. Y. Park, S. Rosenblatt, V. Sazonova, M. Brink, P. L. McEuen: Electrical nanoprobing of semiconducting carbon nanotubes using an atomic force microscope, Phys. Rev. Lett. **92**, 046401 (2004) 460
[16] S. Heinze, J. Tersoff, R. Martel, V. Derycke, J. Appenzeller, P. Avouris: Carbon nanotubes as Schottky barrier transistors, Phys. Rev. Lett. **89**, 106801 (2002) 460, 461
[17] F. Leonard, J. Tersoff: Role of Fermi-level pinning in nanotube Schottky diodes, Phys. Rev. Lett. **84**, 4693–4696 (2000) 460
[18] X. D. Cui, M. Freitag, R. Martel, L. Brus, P. Avouris: Controlling energy-level alignments at carbon nanotube/Au contacts, Nano Lett. **3**, 783–787 (2003) 461
[19] Z. H. Chen, J. Appenzeller, J. Knoch, Y. M. Lin, P. Avouris: The role of metal-nanotube contact in the performance of carbon nanotube field-effect transistors, Nano Lett. **5**, 1497–1502 (2005) 461, 462
[20] W. Kim, A. Javey, R. Tu, J. Cao, Q. Wang, H. J. Dai: Electrical contacts to carbon nanotubes down to 1 nm in diameter, Appl. Phys. Lett. **87**, 173101 (2005) 462
[21] C. Gomez-Navarro, P. J. D. Pablo, J. Gomez-Herrero, B. Biel, F. J. Garcia-Vidal, A. Rubio, F. Flores: Tuning the conductance of single-walled carbon nanotubes by ion irradiation in the Anderson localization regime, Nature Mater. **4**, 534–539 (2005) 463
[22] E. D. Minot, Y. Yaish, V. Sazonova, J. Y. Park, M. Brink, P. L. McEuen: Tuning carbon nanotube band gaps with strain, Phys. Rev. Lett. **90**, 156401 (2003) 463
[23] H. W. C. Postma, T. Teepen, Z. Yao, M. Grifoni, C. Dekker: Carbon nanotube single-electron transistors at room temperature, Science **293**, 76–79 (2001) 463
[24] A. Y. Kasumov, R. Deblock, M. Kociak, B. Reulet, H. Bouchiat, I. Khodos, Y. B. Gorbatov, V. T. Volkov, C. Journet, M. Burghard: Supercurrents through single-walled carbon nanotubes, Science **284**, 1508–1511 (1999) 463, 476
[25] M. T. Woodside, P. L. McEuen: Scanned probe imaging of single-electron charge states in nanotube quantum dots, Science **296**, 1098–1101 (2002) 463, 464
[26] M. Shim, A. Javey, N. W. S. Kam, H. J. Dai: Polymer functionalization for air-stable *n*-type carbon nanotube field-effect transistors, J. Am. Chem. Soc. **123**, 11512–11513 (2001) 463, 466

[27] S. Rosenblatt, Y. Yaish, J. Park, J. Gore, V. Sazonova, P. L. McEuen: High performance electrolyte gated carbon nanotube transistors, Nano Lett. **2**, 869–872 (2002) 463, 466
[28] S. D. Li, Z. Yu, C. Rutherglen, P. J. Burke: Electrical properties of 0.4 cm long single-walled carbon nanotubes, Nano Lett. **4**, 2003–2007 (2004) 463, 466
[29] T. Durkop, S. A. Getty, E. Cobas, M. S. Fuhrer: Extraordinary mobility in semiconducting carbon nanotubes, Nano Lett. **4**, 35–39 (2004) 463, 466
[30] X. J. Zhou, J. Y. Park, S. M. Huang, J. Liu, P. L. McEuen: Band structure, phonon scattering, and the performance limit of single-walled carbon nanotube transistors, Phys. Rev. Lett. **95**, 146805 (2005) 463, 465, 466
[31] T. Ando, T. Nakanishi: Impurity scattering in carbon nanotubes – absence of back scattering, J. Phys. Soc. Jpn. **67**, 1704–1713 (1998) 463
[32] P. L. McEuen, M. Bockrath, D. H. Cobden, Y. G. Yoon, S. G. Louie: Disorder, pseudospins, and backscattering in carbon nanotubes, Phys. Rev. Lett. **83**, 5098–5101 (1999) 463
[33] J. C. Charlier, T. W. Ebbesen, P. Lambin: Structural and electronic properties of pentagon–heptagon pair defects in carbon nanotubes, Phys. Rev. B **53**, 11108–11113 (1996) 464
[34] L. Chico, L. X. Benedict, S. G. Louie, M. L. Cohen: Quantum conductance of carbon nanotubes with defects, Phys. Rev. B **54**, 2600–2606 (1996) 464
[35] L. Chico, V. H. Crespi, L. X. Benedict, S. G. Louie, M. L. Cohen: Pure carbon nanoscale devices: Nanotube heterojunctions, Phys. Rev. Lett. **76**, 971–974 (1996) 464
[36] V. H. Crespi, M. L. Cohen, A. Rubio: In situ band gap engineering of carbon nanotubes, Phys. Rev. Lett. **79**, 2093–2096 (1997) 464
[37] L. Chico, M. P. L. Sancho, M. C. Munoz: Carbon-nanotube-based quantum dot, Phys. Rev. Lett. **81**, 1278–1281 (1998) 464
[38] T. Kostyrko, M. Bartkowiak, G. D. Mahan: Reflection by defects in a tight-binding model of nanotubes, Phys. Rev. B **59**, 3241–3249 (1999) 464
[39] T. Kostyrko, M. Bartkowiak, G. D. Mahan: Localization in carbon nanotubes within a tight-binding model, Phys. Rev. B **60**, 10735–10738 (1999) 464
[40] M. Igami, T. Nakanishi, T. Ando: Conductance of carbon nanotubes with a vacancy, J. Phys. Soc, Jpn. **68**, 716–719 (1999) 464
[41] H. J. Choi, J. Ihm, S. G. Louie, M. L. Cohen: Defects, quasibound states, and quantum conductance in metallic carbon nanotubes, Phys. Rev. Lett. **84**, 2917–2920 (2000) 464
[42] Z. Yao, H. W. C. Postma, L. Balents, C. Dekker: Carbon nanotube intramolecular junctions, Nature **402**, 273–276 (1999) 464, 474
[43] M. Ouyang, J. L. Huang, C. L. Cheung, C. M. Lieber: Atomically resolved single-walled carbon nanotube intramolecular junctions, Science **291**, 97–100 (2001) 464
[44] H. Kim, J. Lee, S. J. Kahng, Y. W. Son, S. B. Lee, C. K. Lee, J. Ihm, Y. Kuk: Direct observation of localized defect states in semiconductor nanotube junctions, Phys. Rev. Lett. **90**, 216107 (2003) 464
[45] B. Gao, D. C. Glattli, B. Placais, A. Bachtold: Cotunneling and one-dimensional localization in individual disordered single-wall carbon nanotubes: Temperature dependence of the intrinsic resistance, Phys. Rev. B **74**, 085410 (2006) 464

[46] J. Zhu, M. Brink, P. L. McEuen: Frequency shift imaging of quantum dots with single-electron resolution, Appl. Phys. Lett. **87**, 242102 (2005) 464
[47] C. L. Kane, E. J. Mele, R. S. Lee, J. E. Fischer, P. Petit, H. Dai, A. Thess, R. E. Smalley, A. R. M. Verschueren, S. J. Tans, C. Dekker: Temperature-dependent resistivity of single-wall carbon nanotubes, Europhys. Lett. **41**, 683–688 (1998) 464
[48] J. Appenzeller, R. Martel, P. Avouris, H. Stahl, B. Lengeler: Optimized contact configuration for the study of transport phenomena in ropes of single-wall carbon nanotubes, Appl. Phys. Lett. **78**, 3313–3315 (2001) 464
[49] J. Y. Park, S. Rosenblatt, Y. Yaish, V. Sazonova, H. Ustunel, S. Braig, T. A. Arias, P. W. Brouwer, P. L. McEuen: Electron–phonon scattering in metallic single-walled carbon nanotubes, Nano Lett. **4**, 517–520 (2004) 464
[50] Z. Yao, C. L. Kane, C. Dekker: High-field electrical transport in single-wall carbon nanotubes, Phys. Rev. Lett. **84**, 2941–2944 (2000) 464
[51] A. Javey, J. Guo, M. Paulsson, Q. Wang, D. Mann, M. Lundstrom, H. J. Dai: High-field quasiballistic transport in short carbon nanotubes, Phys. Rev. Lett. **92**, 106804 (2004) 464, 476
[52] A. Javey, P. F. Qi, Q. Wang, H. J. Dai: Ten- to 50-nm-long quasi-ballistic carbon nanotube devices obtained without complex lithography, Proc. Nat. Acad. Sci. USA **101**, 13408–13410 (2004) 464
[53] E. Pop, D. Mann, J. Cao, Q. Wang, K. Goodson, H. J. Dai: Negative differential conductance and hot phonons in suspended nanotube molecular wires, Phys. Rev. Lett. **95**, 155505 (2005) 465
[54] D. Mann, Y. K. Kato, A. Kinkhabwala, E. Pop, J. Cao, X. R. Wang, L. Zhang, Q. Wang, J. Guo, H. J. Dai: Electrically driven thermal light emission from individual single-walled carbon nanotubes, Nature Nanotechnol. **2**, 33–38 (2007) 465
[55] H. Suzuura, T. Ando: Phonons and electron-phonon scattering in carbon nanotubes, Phys. Rev. B **65**, 235412 (2002) 466
[56] G. Pennington, N. Goldsman: Semiclassical transport and phonon scattering of electrons in semiconducting carbon nanotubes, Phys. Rev. B **68**, 045426 (2003) 466
[57] V. Perebeinos, J. Tersoff, P. Avouris: Electron–phonon interaction and transport in semiconducting carbon nanotubes, Phys. Rev. Lett. **94**, 086802 (2005) 466
[58] A. Javey, H. Kim, M. Brink, Q. Wang, A. Ural, J. Guo, P. McIntyre, P. McEuen, M. Lundstrom, H. J. Dai: High-kappa dielectrics for advanced carbon-nanotube transistors and logic gates, Nature Mater. **1**, 241–246 (2002) 467, 468
[59] A. Javey, J. Guo, D. B. Farmer, Q. Wang, E. Yenilmez, R. G. Gordon, M. Lundstrom, H. J. Dai: Self-aligned ballistic molecular transistors and electrically parallel nanotube arrays, Nano Lett. **4**, 1319–1322 (2004) 467
[60] S. J. Wind, J. Appenzeller, R. Martel, V. Derycke, P. Avouris: Vertical scaling of carbon nanotube field-effect transistors using top gate electrodes, Appl. Phys. Lett. **80**, 3817–3819 (2002) 467
[61] A. Javey, J. Guo, D. B. Farmer, Q. Wang, D. W. Wang, R. G. Gordon, M. Lundstrom, H. J. Dai: Carbon nanotube field-effect transistors with integrated ohmic contacts and high-k gate dielectrics, Nano Lett. **4**, 447–450 (2004) 467

[62] Z. H. Chen, J. Appenzeller, Y. M. Lin, J. Sippel-Oakley, A. G. Rinzler, J. Y. Tang, S. J. Wind, P. M. Solomon, P. Avouris: An integrated logic circuit assembled on a single carbon nanotube, Science **311**, 1735–1735 (2006) 467, 469
[63] Z. Yu, P. J. Burke: Microwave transport in metallic single-walled carbon nanotubes, Nano Lett. **5**, 1403–1406 (2005) 469
[64] J. J. Plombon, K. P. O'Brien, F. Gstrein, V. M. Dubin, Y. Jiao: High-frequency electrical properties of individual and bundled carbon nanotubes, Appl. Phys. Lett. **90**, 063106 (2007) 469
[65] Z. Yu, C. Rutherglen, R. J. Burke: Microwave nanotube transistor operation at high bias, Appl. Phys. Lett. **88**, 233115 (2006) 469
[66] S. D. Li, Z. Yu, S. F. Yen, W. C. Tang, P. J. Burke: Carbon nanotube transistor operation at 2.6 GHz, Nano Lett. **4**, 753–756 (2004) 469
[67] M. J. Biercuk, D. J. Reilly, T. M. Buehler, V. C. Chan, J. M. Chow, R. G. Clark, C. M. Marcus: Charge sensing in carbon-nanotube quantum dots on microsecond timescales, Phys. Rev. B **73**, 201402 (2006) 469, 485
[68] V. Sazonova, Y. Yaish, H. Ustunel, D. Roundy, T. A. Arias, P. L. McEuen: A tunable carbon nanotube electromechanical oscillator, Nature **431**, 284–287 (2004) 470, 471
[69] J. Appenzeller, D. J. Frank: Frequency dependent characterization of transport properties in carbon nanotube transistors, Appl. Phys. Lett. **84**, 1771–1773 (2004) 470
[70] S. Rosenblatt, H. Lin, V. Sazonova, S. Tiwari, P. L. McEuen: Mixing at 50 GHz using a single-walled carbon nanotube transistor, Appl. Phys. Lett. **87**, 153111 (2005) 470, 485
[71] A. A. Pesetski, J. E. Baumgardner, E. Folk, J. X. Przybysz, J. D. Adam, H. Zhang: Carbon nanotube field-effect transistor operation at microwave frequencies, Appl. Phys. Lett. **88**, 113103 (2006) 470
[72] F. Rodriguez-Morales, R. Zannoni, J. Nicholson, M. Fischetti, K. S. Yngvesson, J. Appenzeller: Direct and heterodyne detection of microwaves in a metallic single wall carbon nanotube, Appl. Phys. Lett. **89**, 083502 (2006) 470
[73] H. B. Peng, C. W. Chang, S. Aloni, T. D. Yuzvinsky, A. Zettl: Ultrahigh frequency nanotube resonators, Phys. Rev. Lett. **97**, 087203 (2006) 470
[74] B. Witkamp, M. Poot, H. S. J. van der Zant: Bending-mode vibration of a suspended nanotube resonator, Nano Lett. **6**, 2904–2908 (2006) 470
[75] S. J. Kang, C. Kocabas, T. Ozel, M. Shim, N. Pimparkar, M. A. Alam, S. V. Rotkin, J. A. Rogers: High-performance electronics using dense, perfectly aligned arrays of single-walled carbon nanotubes, Nature Nanotechnol. **2**, 230–236 (2007) 470
[76] E. S. Snow, J. P. Novak, P. M. Campbell, D. Park: Random networks of carbon nanotubes as an electronic material, Appl. Phys. Lett. **82**, 2145–2147 (2003) 470
[77] J. U. Lee, P. P. Gipp, C. M. Heller: Carbon nanotube p–n junction diodes, Appl. Phys. Lett. **85**, 145–147 (2004) 470, 472
[78] K. Bosnick, N. Gabor, P. McEuen: Transport in carbon nanotube p–i–n diodes, Appl. Phys. Lett. **89**, 163121 (2006) 470

[79] E. D. Minot, Y. Yaish, V. Sazonova, P. L. McEuen: Determination of electron orbital magnetic moments in carbon nanotubes, Nature **428**, 536–539 (2004) 472, 473
[80] W. J. Liang, M. Bockrath, H. Park: Transport spectroscopy of chemical nanostructures: The case of metallic single-walled carbon nanotubes, Ann. Rev. Phys. Chem. **56**, 475–490 (2005) 474, 475
[81] F. D. M. Haldane: 'Luttinger liquid theory' of one-dimensional quantum fluids. I. Properties of the Luttinger model and their extension to the general 1D interacting spinless Fermi gas, J. Phys. C **14**, 2585–609 (1981) 474
[82] J. Voit: One-dimensional Fermi liquids, Rep. Prog. Phys. **57**, 977 (1994) 474
[83] M. Bockrath, D. H. Cobden, J. Lu, A. G. Rinzler, R. E. Smalley, T. Balents, P. L. McEuen: Luttinger-liquid behaviour in carbon nanotubes, Nature **397**, 598–601 (1999) 475
[84] H. W. C. Postma, M. de Jonge, C. Dekker: Electrical transport through carbon nanotube junctions created by mechanical manipulation, Phys. Rev. B **62**, R10653–6 (2000) 475
[85] D. Mann, A. Javey, J. Kong, Q. Wang, H. Dai: Ballistic transport in metallic nanotubes with reliable Pd ohmic contacts, Nano Lett. **3**, 1541 (2003) 476
[86] C. Berger, Y. Yi, Z. L. Wang, W. A. de Heer: Multiwalled carbon nanotubes are ballistic conductors at room temperature, Appl. Phys. A-Mater. **A74**, 363–5 (2002) 476
[87] C. Berger, P. Poncharal, Y. Yi, W. de Heer: Ballistic conduction in multiwalled carbon nanotubes, J. Nanosci. Nanotechnol. **3**, 171–7 (2003) 476
[88] H. van Houten, C. Beenakker, B. van Wees: in M. A. Reed (Ed.): *Nanostructured Systems* (Academic Press, San Diego 1992) pp. 9–112 476
[89] W. Liu, J. Xiang, B. P. Timko, Y. Wu, C. M. Lieber: One-dimensional hole gas in germanium/silicon nanowire heterostructures, Proc. Nat. Acad. Sci. **102**, 10046 (2005) 476
[90] D. J. Reilly, T. M. Buehler, J. L. O'Brien, A. R. Hamilton, A. S. Dzurak, R. G. Clark, B. E. Kane, L. N. Pfeiffer, K. W. West: Density-dependent spin polarization in ultra-low-disorder quantum wires, Phys. Rev. Lett. **89**, 246801/1–4 (2002) 476
[91] K. J. Thomas, J. T. Nicholls, M. Y. Simmons, M. Pepper, D. R. Mace, D. A. Ritchie: Possible spin polarization in a one-dimensional electron gas, Phys. Rev. Lett. **77**, 135–8 (1996) 476
[92] G. Scappucci, L. D. Gaspare, E. Giovine, A. Notargiacomo, R. Leoni, F. Evangelisti: Conductance quantization in etched Si/SiGe quantum point contacts, Phys. Rev. B **74**, 035321 (2006) 476
[93] S. M. Cronenwett, H. J. Lynch, D. Goldhaber-Gordon, L. P. Kouwenhoven, C. M. Marcus, K. Hirose, N. S. Wingreen, V. Umansky: Low-temperature fate of the 0.7 structure in a point contact: A Kondo-like correlated state in an open system, Phys. Rev. Lett. **88**, 226805/1–4 (2002) 476
[94] A. F. Morpurgo, J. Kong, C. M. Marcus, H. Dai: Gate-controlled superconducting proximity effect in carbon nanotubes, Science **286**, 263–5 (1999) 476
[95] P. Jarillo-Herrero, J. A. van Dam, L. P. Kouwenhoven: Quantum supercurrent transistors in carbon nanotubes, Nature **439**, 953 (2006) 476, 477, 478, 481
[96] J. P. Cleuziou, W. Wernsdorfer, S. Andergassen, S. Florens, V. Bouchiat, T. Ondarcuhu, M. Monthioux: Gate-tuned high frequency response of carbon nanotube Josephson junctions, arXiv (2007) URL: `0705.2033` 477

[97] J. P. Cleuziou, W. Wernsdorfer, H. Bouchiat, T. Ondarcuhu, M. Monthioux: Carbon nanotube superconducting quantum interference device, Nature Nanotechnol. **1**, 53 (2006) 477
[98] S. Chakraborty, K. M. Walsh, B. W. Alphenaar, L. Liu, K. Tsukagoshi: Temperature-mediated switching of magnetoresistance in co-contacted multiwall carbon nanotubes, Appl. Phys. Lett. **83**, 1008–10 (2003) 478
[99] K. Tsukagoshi, B. W. Alphenaar, H. Ago: Coherent transport of electron spin in a ferromagnetically contacted carbon nanotube, Nature **401**, 572–4 (1999) 478
[100] S. Sahoo, T. Kontos, C. Schonenberger, C. Surgers: Electrical spin injection in multiwall carbon nanotubes with transparent ferromagnetic contacts, Appl. Phys. Lett. **86**, 112109 (2005) 478, 481
[101] H. T. Man, I. J. W. Wever, A. F. Morpurgo: Spin-dependent quantum interference in single-wall carbon nanotubes with ferromagnetic contacts, Phys. Rev. B **73**, 241401(R) (2006) 478, 479
[102] A. Cottet, T. Kontos, S. Sahoo, H. T. Man, M.-S. Choi, W. Belzig, C. Bruder, A. F. Morpurgo, C. Schonenberger: Nanospintronics with carbon nanotubes, Semicond. Sci. Technol. **21**, S78 (2006) 478, 481
[103] C. Beenakker, H. van Houten: in *Solid State Physics – Advances in Research and Applications* (Academic, San Diego, CA 1991) pp. 1–228 478
[104] L. Kouwenhoven, C. Marcus: Quantum dots, Phys. World **11**, 35–9 (1998) 479
[105] L. P. Kouwenhoven, C. Marcus, P. L. McEuen, S. Tarucha, R. M. Westervelt, N. S. Wingreen: Electron transport in quantum dots, in L. P. Kouwenhoven, G. Schon, L. L. Sohn (Eds.): *NATO ASI conference proceedings* (Kluwer, Dordrecht 1997) 480
[106] D. H. Cobden, M. Bockrath, P. L. McEuen, A. G. Rinzler, R. E. Smalley: Spin splitting and even-odd effects in carbon nanotubes, Phys. Rev. Lett. **81**, 681–4 (1998) 480
[107] D. H. Cobden, J. Nygard: Shell filling in closed single-wall carbon nanotube quantum dots, Phys. Rev. Lett. **89**, 046803 (2002) 481
[108] W. Liang, M. Bockrath, H. Park: Shell filling and exchange coupling in metallic single-walled carbon nanotubes, Phys. Rev. Lett. **88**, 126801/1–4 (2002) 481
[109] S. Sapmaz, P. Jarillo-Herrero, J. Kong, C. Dekker, L. P. Kouwenhoven, H. S. J. van der Zant: Electronic excitation spectrum of metallic carbon nanotubes, Phys. Rev. B **71**, 153402 (2005) 481
[110] P. Jarillo-Herrero, J. Kong, H. S. J. van der Zant, C. Dekker, L. P. Kouwenhoven, S. D. Franceschi: Orbital Kondo effect in carbon nanotubes, Nature **434**, 484 (2005) 481, 482, 483
[111] A. Makarovski, J. Liu, G. Finkelstein: Evolution of SU(4) transport regimes in carbon nanotube quantum dots, arXiv (2006) URL: `cond-mat/0608573` 481
[112] S. Moriyama, T. Fuse, M. Suzuki, Y. Aoyagi, K. Ishibashi: Four-electron shell structures and an interacting two-electron system in carbon nanotube quantum dots, Phys. Rev. Lett. **94**, 186806 (2005) 481
[113] S. Sahoo, T. Kontos, J. Furer, C. Hoffmann, M. Graber, A. Cottet, C. Schonenberger: Electric field control of spin transport, Nature Phys. **1**, 99 (2005) 481

[114] A. C. Hewson: *The Kondo Problem to Heavy Fermion* (Cambridge University Press, Cambridge 1993) 481
[115] L. Kouwenhoven, L. Glazman: Revival of the Kondo effect, Phys. World **14**, 33–38 (2001) 481
[116] J. Nygard, D. H. Cobden, P. E. Lindelof: Kondo physics in carbon nanotubes, Nature **408**, 342–6 (2000) 481
[117] J. Paaske, A. Rosch, P. Wolfle, N. Mason, C. Marcus, J. Nygard: Non-equilibrium singlet–triplet Kondo effect in carbon nanotubes, Nature Phys. **2**, 460 (2006) 482
[118] A. A. Clerk, V. Ambegaokar, S. Hershfield: Andreev scattering and the Kondo effect, Phys. Rev. B **61**, 3555–62 (2000) 482
[119] M. R. Buitelaar, W. Belzig, T. Nussbaumer, B. Babic, C. Bruder, C. Schonenberger: Multiple Andreev reflections in a carbon nanotube quantum dot, Phys. Rev. Lett. **91**, 057005 (2003) 482
[120] M. Graber, T. Nussbaumer, W. Belzig, C. Schonenberger: Quantum dot coupled to a normal and a superconducting lead, Nanotechnol. **15**, S479 (2004) 483
[121] M. J. Biercuk, N. Mason, C. M. Marcus: Locally addressable tunnel barriers within a carbon nanotube, Nano Lett. **4**, 2499–2502 (2004) 483
[122] M. J. Biercuk, S. Garaj, N. Mason, J. M. Chow, C. M. Marcus: Gate-defined quantum dots on carbon nanotubes, Nano Lett. **5**, 1267 (2005) 483, 484
[123] S. Sapmaz, C. Meyer, P. Beliczynski, P. Jarillo-Herrero, L. P. Kouwenhoven: Excited state spectroscopy in carbon nanotube double quantum dots, Nano Lett. **6**, 1350 (2006) 483, 484
[124] M. Graber, T. Nussbaumer, W. Belzig, C. Schonenberger: Molecular states in carbon nanotube double quantum dots, Phys. Rev. B **74**, 075427 (2006) 483
[125] H. I. Grove-Rasmussen, J. R. Hauptmann, P. E. Lindelof: Single wall carbon nanotube double quantum dot, Appl. Phys. Lett. **89**, 232113 (2006) 483
[126] Y. G. Semenov, K. W. Kim, G. J. Iafrate: Electron spin relaxation in semiconducting carbon nanotubes: The role of hyperfine interaction, Phys. Rev. B **75**, 045429 (2007) 485
[127] P. J. Burke: Solid State Electronics **48**, 2013 (2004) 485

Index